Remote Sensing of Environment 257 (2021) 112337

Contents lists available at ScienceDirect

Remote Sensing of Environment

journal homepage: www.elsevier.com/locate/rse

Phenological corrections to a field-scale, ET-based crop stress indicator: An application to yield forecasting across the U.S. Corn Belt

Yang Yang [a,*], Martha C. Anderson [a], Feng Gao [a], David M. Johnson [b], Yun Yang [a], Liang Sun [c], Wayne Dulaney [a], Christopher R. Hain [d], Jason A. Otkin [e], John Prueger [f], Tilden P. Meyers [g], Carl J. Bernacchi [h,i,j], Caitlin E. Moore [k,l]

[a] USDA ARS, Hydrology and Remote Sensing Laboratory, Beltsville, MD, USA
[b] USDA NASS, Research and Development Division, Washington, DC, USA
[c] Institute of Agricultural Resources and Reginal Planning, Chinese Academy of Agricultural Sciences, Key Laboratory of Agricultural Remote Sensing, Ministry of Agriculture Beijing, China
[d] Marshall Space Flight Center, Earth Science Branch, Huntsville, AL, USA
[e] Space Science and Engineering Center, University of Wisconsin-Madison, WI, USA
[f] USDA ARS, National Laboratory for Agriculture and The Environment, Ames, IA, USA
[g] Atmospheric Turbulence and Diffusion Division, National Oceanic and Atmospheric Administration, Oak Ridge, TN, USA
[h] Department of Plant Biology, University of Illinois at Urbana-Champaign, USA
[i] Carl R Woese Institute for Genomic Biology, University of Illinois at Urbana-Champaign, USA
[j] USDA ARS Global Change and Photosynthesis Research Unit, Urbana, IL, USA
[k] Institute for Sustainability, Energy and Environment, University of Illinois at Urbana-Champaign, IL, USA
[l] School of Agriculture and Environment, University of Western Australia, Crawley, WA, Australia

ARTICLE INFO

Keywords:
evaporative stress index (ESI)
Evapotranspiration (ET)
Yield
Phenology
Corn Belt

ABSTRACT

Soil moisture deficiency is a major factor in determining crop yields in water-limited agricultural production regions. Evapotranspiration (ET), which consists of crop water use through transpiration and water loss through direct soil evaporation, is a good indicator of soil moisture availability and vegetation health. ET therefore has been an integral part of many yield estimation efforts. The Evaporative Stress Index (ESI) is an ET-based crop stress indicator that describes temporal anomalies in a normalized evapotranspiration metric as derived from satellite remote sensing. ESI has demonstrated the capacity to explain regional yield variability in water-limited regions. However, its performance in some regions where the vegetation cycle is intensively managed appears to be degraded due to interannual phenological variability. This investigation selected three study sites across the U.S. Corn Belt – Mead, NE, Ames, IA and Champaign, IL – to investigate the potential operational value of 30-m resolution, phenologically corrected ESI datasets for yield prediction. The analysis was conducted over an 8-year period from 2010 to 2017, which included both drought and pluvial conditions as well as a broad range in yield values. Detrended yield anomalies for corn and soybean were correlated with ESI computed using annual ET curves temporally aligned based on (1) calendar date, (2) crop emergence date, and (3) a growing degree day (GDD) scaled time axis. Results showed that ESI has good correlations with yield anomalies at the county scale and that phenological corrections to the annual temporal alignment of the ET timeseries improve the correlation, especially when the time axis is defined by GDD rather than the calendar date. Peak correlations occur in the silking stage for corn and the reproductive stage for soybean – phases when these crops are particularly sensitive to soil moisture deficiencies. Regression equations derived at the time of peak correlation were used to estimate yields at county scale using a leave-one-out cross-validation strategy. The ESI-based yield estimates agree well with the USDA National Agricultural Statistics Service (NASS) county-level crop yield data, with correlation coefficients ranging from 0.79 to 0.93 and percent root-mean-square errors of 5–8%. These results demonstrate that remotely sensed ET at high spatiotemporal resolution can convey valuable water stress information for forecasting crop yields across the Corn Belt if interannual phenological variability is considered.

* Corresponding author at: 10300 Baltimore Ave, Beltsville, MD 20705, USA.
E-mail address: yang.yang@usda.gov (Y. Yang).

https://doi.org/10.1016/j.rse.2021.112337
Received 29 April 2020; Received in revised form 29 January 2021; Accepted 1 February 2021
Available online 23 February 2021

1. Introduction

Globally, soil water deficits are the single most important factor limiting crop yield (Begg and Turner 1976). Numerous indicators based on precipitation, soil moisture, vegetation indices (e.g. the Normalized Difference Vegetation Index; NDVI), and evapotranspiration (ET) have been used to quantify crop water stress and its relationship to yield. Among these indicators, ET uniquely integrates multiple factors relevant to yield response (i.e., soil moisture, climate, biomass, and crop condition) and is intimately connected to crop moisture availability. As early as the 1960s, Jensen (1968) demonstrated the strong linkage between crop yield and the ratio of actual-to-reference ET (f_{RET}), serving as a proxy for moisture stress. Inspired by this work, Doorenbos and Kassam (1979) established relationships between relative yield losses and relative water deficits during different phases of crop growth using coefficients derived from ET.

Until recently, spatially explicit maps of ET and f_{RET} have not been extensively used for crop stress monitoring and crop yield estimation. Advances in remote sensing retrieval techniques over a range of spatial scales have produced ET-based metrics that have been identified as valuable indicators of crop water stress (Moran 2004). However, few studies have focused on exploring the use of remote sensing-based ET retrieval to estimate crop yield. Spatially explicit ET data have been related to yield by empirical regressions or correlation analyses (Anderson et al. 2016a, 2016b; Tadesse et al. 2015; Yang et al. 2018) or by integration into process-based models (Bastiaanssen and Ali 2003; Huang et al. 2015; Mishra et al. 2013; Teixeira et al. 2013).

The Evaporative Stress Index (ESI) was specifically designed to identify stress conditions associated with agricultural drought (Anderson et al. 2007a, 2016b). The ESI represents temporal anomalies in f_{RET}, which is retrieved from remotely sensed land-surface temperature (LST) data using the Atmosphere-Land Exchange Inverse (ALEXI) surface energy balance algorithm (Anderson et al. 2007a, 2011, 2013). Given the linkage between f_{RET} and root-zone soil moisture availability in vegetated areas (Hain et al. 2009, 2011), the ESI has been shown to provide enhanced early warning of deteriorating crop moisture conditions (i.e., flash drought) when compared with precipitation or VI-based indices (Anderson et al. 2011, 2013, 2015; Otkin et al. 2013, 2014). In addition, the ET-based ESI index has also demonstrated the capability to explain yield variability in regional- and field-scale studies (Anderson et al. 2016a, 2016b; Mladenova et al. 2017; Otkin et al. 2016; Yang et al. 2018). Operational ESI product archives are currently being developed over the United States and globally at 4–10 km resolution using time-differential thermal infrared (TIR) imagery from geostationary (Anderson et al. 2013) or polar orbiting (Hain and Anderson 2017) satellites.

Although the regional ESI shows good agreement with other drought indicators that are based on precipitation and rainfall, as well as with drought severity patterns seen in the U.S. Drought Monitor, Anderson et al. (2013) noted increased noise in a 10-km resolution ESI product over intensively managed agricultural lands in the heart of the U.S. Corn Belt (see e.g., their Fig. 10). This noise was attributed to the strongly peaked seasonal curve in f_{RET} in this region - small shifts in phenology from year-to-year (e.g., differing emergence dates) result in large temporal anomalies that are not necessarily related to crop stress. Further degradation in the ESI signal may result from the inclusion of multiple crop and land-cover types at the 10-km pixel scale, each with a different characteristic phenological cycle.

In order to detect the effect of phenological behavior on crop water use, and to reduce its impact on the diagnosed stress signal, Yang et al. (2018) conducted a high-resolution assessment of ESI correlations with crop yield at the field scale. This investigation used an ALEXI disaggregation algorithm (DisALEXI; Norman et al. 2003; Anderson et al. 2004), which spatially downscales regional ALEXI fluxes based on finer-scale thermal imagery from sensors like Landsat (30-m with sharpening/8–16 day revisit) and MODIS (500-m/~daily acquisition). A data fusion technique is then used to combine Landsat and MODIS ET image timeseries to generate high spatiotemporal resolution ET datacubes of 30-m pixels and a daily timestep. Yang et al. (2018) used 5-year ET datacubes of 35 × 35 km extent developed over experimental fields near Mead, NE to demonstrate that by selecting pure, single crop pixels and correcting for year-to-year variations in field-observed crop emergence date, correlations between ESI and yield improved from 0.28 at the 4-km scale to 0.93 at the 30-m scale.

The current investigation builds on the study of Yang et al. (2018) by extending the analysis to multiple sites, larger areas, longer timeframes, and season-wide phenological alignment strategies to further assess the potential operational value of 30-m ESI datasets for yield prediction. Thirty-meter ET datacubes were constructed over three sites across the U.S. Corn Belt –near Mead, NE, Ames, IA and Champaign, IL, allowing for sampling a broader range of climate and water management practices. The analysis was conducted over an 8-year period from 2010 to 2017, which was characterized by both drought and pluvial conditions and a large range in yield values. Retrieved ET timeseries extracted from each datacube are evaluated with respect to long-term flux tower observations collected over corn and soybean crops to provide an assessment of the accuracy in the baseline flux retrievals. Next, interannual variations in corn and soybean yield, emergence date and primary climatic driving factors (precipitation and temperature) are assessed across all sites and years to establish context. Relationships between crop-specific ESI and county-level yield data are assessed with and without phenological correction for emergence date. We also evaluate correction of the post-emergence timescale by using growing degree-days (GDDs), rather than calendar date, to account for variations in temperature-induced crop growth rate from year to year (Qian et al. 2019). Finally, ESI-yield regression relations derived from sample datasets at times of peak correlation are used to evaluate the effect of phenology corrections on the accuracy of resulting yield estimates.

2. Study domains

The U.S. Corn Belt roughly spans across 10 Midwest states (South Dakota, Nebraska, Kansas, Minnesota, Iowa, Missouri, Wisconsin, Illinois, Indiana, and Ohio), a region characterized by a large east-west precipitation gradient resulting in diverse agricultural practices. These ten states produced more than 80% of the U.S. corn crop over the past five years (NASS Quick Stats, 2010-2019). To test the variability in yield – ESI correlations across the Corn Belt, three sites (Mead, NE; Ames, IA; Champaign, IL; Fig. 1) were selected, representing growing conditions with increasing precipitation and decreasing irrigation intensity from west to east. Land use in the three sites is primarily agricultural with alternating years of corn and soybean crops. These modeling sites were selected (1) based on the availability of multiple flux towers with high quality, long-term records and yield biophysical measurements; and (2) to sample the predominant ET gradient across the Corn Belt resulting from varying climate and agricultural water management practices.

For each study site, a modeling domain of approximately 90 × 90 km, covering approximately 5–6 counties, was defined that included the target tower sites (Fig. 1). Thirty-meter resolution daily ET datacubes were constructed for each site for the period 2010–2017. The general characteristics of the sites and drought conditions over the study period are described in Sec 2.1–2.2, while details regarding the flux tower observations are provided in Sec. 4.1.

2.1. Study sites

The Mead, NE study area, covering parts of six counties, is primarily characterized by corn and soybean rotations with a mixture of irrigated and rain-fed fields. Croplands account for more than 85% of the total area within the modeling domain, and irrigation practices have significantly increased in the eastern part of Nebraska during the past three decades (Deines et al. 2019). The climate is humid continental, with an annual average temperature of 10.5 °C and an annual precipitation total of 785 mm.

The study area around Ames, IA includes parts of five counties supporting rain-fed corn and soybean production (83% of the total landcover), typically grown in rotation in consecutive years. The average annual temperature in the Ames study area is 8.9 °C with an average annual rainfall of 845 mm.

Agriculture in the Champaign, IL study area, extending over parts of six counties, is mostly rain-fed, cultivated with alternating years of soybean and corn crops that account for 88% of the total study area. The area has a climate classification of humid continental, with an annual average temperature of 11 °C and an annual precipitation total of 990 mm.

2.2. Climate conditions over the study period

Due to the gradients in rainfall and water management practices that span the Corn Belt, crops grown in these three study sites are susceptible to periodic drought to differing degrees. Drought conditions at each site from 2010 to 2017, as characterized by the U.S. Drought Monitor (USDM) time series (http://www.droughtmonitor.unl.edu/Data/Timeseries.aspx) and regional GOES-based ESI, are shown in Fig. 2. The USDM classifies drought into five drought severity classes (i.e., D0: abnormally dry, D1: moderate drought, D2: severe drought, D3: extreme drought, and D4: exceptional drought). The ESI maps are computed from 4-week composites at 4-km resolution. Also shown is the temporal evolution over the study period of percent area covered by each USDM class within the hydrologic unit code (HUC) region that encompasses each study domain and surrounding areas (102,002, 070802, 071300 for Mead, Ames and Champaign, respectively).

In 2012, most of the Corn Belt was affected by a flash drought, with rapid onset starting in mid-May. Otkin et al. (2016) identified the classic ESI flash drought signature in 2012, characterized by a pulse of high ET in April-early May as soil moisture reserves rapidly deplete followed by a steep trajectory toward negative (i.e., stressed) ESI. Fig. 2 shows that the Mead site was most strongly impacted by the 2012 drought, with a large percentage of the area under extreme drought (D3) for almost six months and 20% of the area was under exceptional drought (D4) for five months. In contrast, drought conditions in Ames and Champaign were not quite as severe in 2012, instead peaking at D3. As shown by Otkin et al. (2016), the ESI tracked the spatiotemporal patterns of USDM and

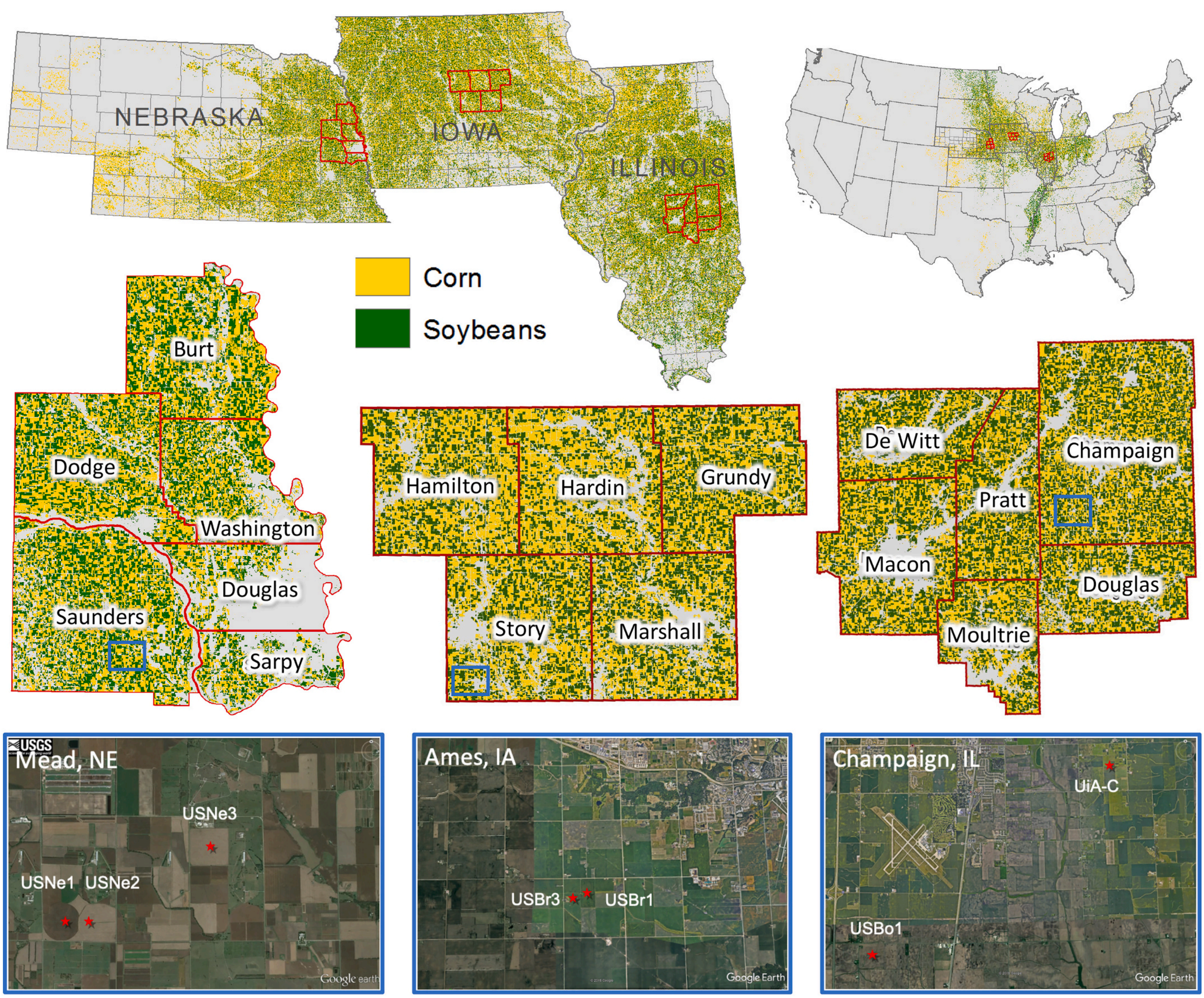

Fig. 1. Study domains cover several counties outlined by red line. Background map in the top two rows is from the NASS 2017 Cropland Data Layer, showing corn and soybean cropped area. Flux tower locations are marked in red on true colour images from Google Earth shown in the bottom row. (For interpretation of the references to colour in this figure legend, the reader is referred to the web version of this article.)

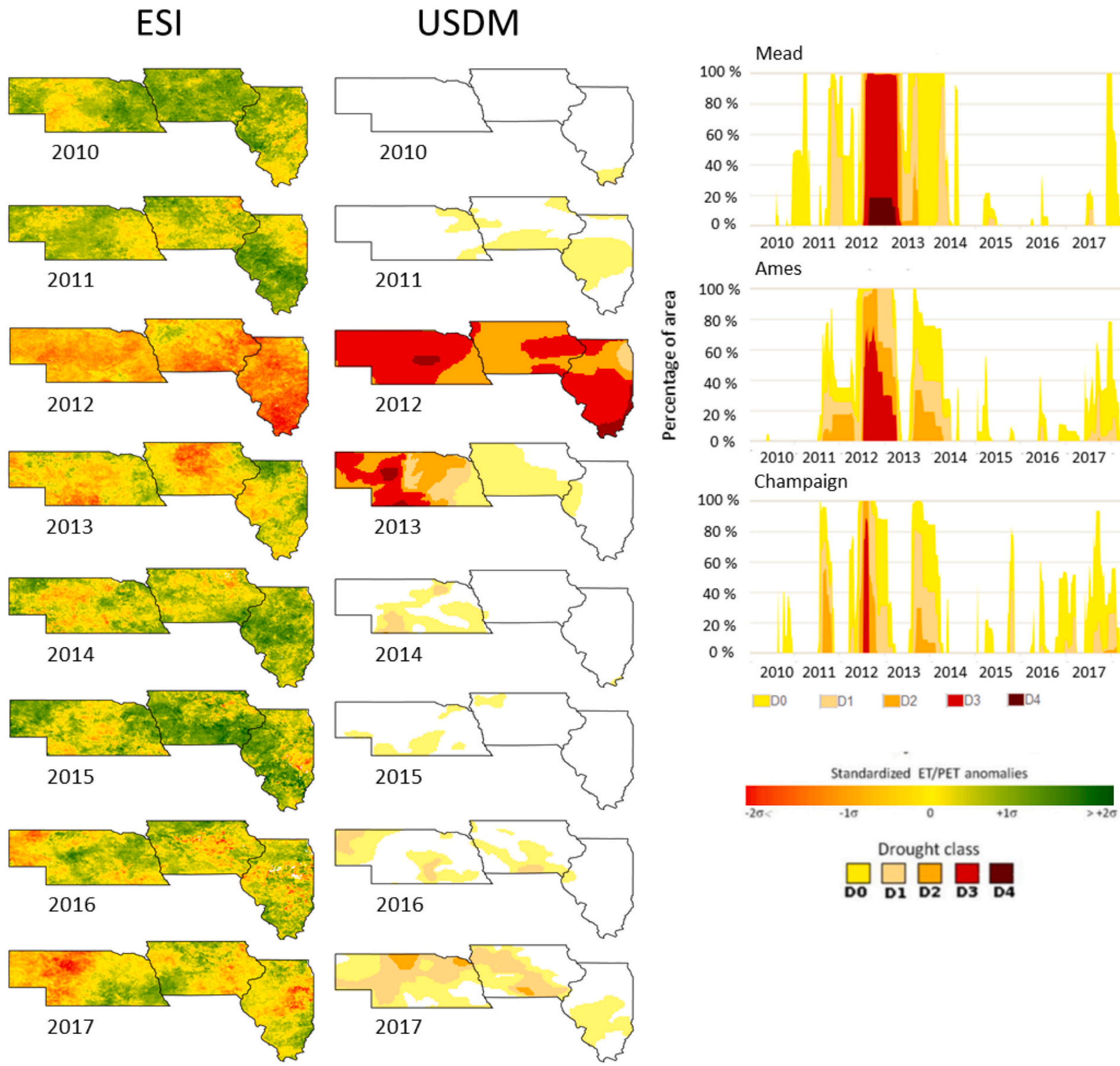

Fig. 2. Annual ESI (4-wk) and USDM 2010–2017 maps from the end of July for NE, IL and IA (left two columns), and timeseries of USDM drought classification areal percentages in the HUC region containing the Mead, Ames, and Champaign study domains (right column). D0 indicates abnormally dry, D1 is moderate drought, D2 is severe drought, D3 is extreme drought, and D4 is an exceptional drought.

NASS crop conditions in 2012 well. Drought of varying degrees persisted through 2013 at the three study areas. All three study areas were also impacted by D0-D1 drought in 2017.

3. Methods

3.1. ET retrieval based on energy balance

The Atmosphere-Land Exchange Inverse (ALEXI) surface energy balance model (Anderson et al. 1997, 2007a) and associated flux disaggregation algorithm (DisALEXI; Anderson et al. 2004; Norman et al. 2003) are used in this study to retrieve ET at different spatio-temporal scales. In ALEXI, a simple slab model of energy conservation in the atmospheric boundary layer (McNaughton and Spriggs 1986), is coupled with the Two-Source Energy Balance (TSEB) model (Kustas and Norman 1999; Norman et al. 1995) to partition the surface energy budget:

$$R_n = H + \lambda E + G \tag{1}$$

where Rn is net radiation, λE is latent heat, H is sensible heat, and G is the soil heat flux (all in units of Wm^{-2}). Primary remote sensing inputs are land surface temperature (LST), used to constrain energy balance, and vegetation cover fraction governing the partitioning between soil and canopy flux sources.

ALEXI uses time-differential measurements of the morning LST rise, typically acquired by geostationary satellites with resolutions from 3 to 10 km. Finer scale assessments of ET can be obtained using the DisALEXI algorithm (Norman et al. 2003, Anderson et al. 2012), which spatially downscales regional ALEXI latent heat flux by applying the TSEB to higher resolution LST data retrieved from thermal infrared (TIR) imagery collected on airborne or polar orbiting satellite platforms. To ensure consistency between spatial scales, the DisALEXI air temperature boundary conditions are iteratively adjusted until the disaggregated daily ET fluxes match the ALEXI flux baseline at the ALEXI pixel scale. Additional details are given in Sun et al. (2017).

Instantaneous latent heat flux estimates at the satellite observation time are integrated to daily values and converted to mass flux (ET) by conserving the ratio between evapotranspiration and insolation:

$$f_{inst} = \frac{\lambda E_{inst}}{Rs_{inst}} \tag{2}$$

$$ET_d = \frac{f_{inst} * Rs_{24}}{\lambda * \rho_w} \tag{3}$$

where f_{inst} is the ratio of instantaneous latent heat to instantaneous insolation at the satellite overpass time, and Rs_{24} is the time-integrated daily (24-h) insolation rate (Cammalleri et al. 2014). The latent heat energy flux is converted to an ET mass flux using the latent heat of evaporation (λ) and the density of water (ρ_w).

3.2. ET data fusion

To create the sub-field scale ET datacubes (30-m/daily) used in this study, high temporal/low spatial resolution MODIS imagery (500-m/~daily acquisition) and low temporal/high spatial resolution Landsat (30-m/periodic acquisition) ETd image timeseries were generated with DisALEXI and then fused using the Spatial and Temporal Adaptive Reflectance Fusion Model (STARFM; Gao et al. 2006, 2015). STARFM computes a spatially distributed weighting function from MODIS and Landsat image pairs on those days when both are available and applies these weights to downscale MODIS images to the Landsat scale between Landsat overpasses. For details regarding the ET data fusion process, the reader is referred to Cammalleri et al. (2014), Sun et al. (2017), and Yang et al. (2017). For this project, eight years of daily, 30-m resolution ET imagery were constructed over the three target domains.

3.3. Regional ALEXI-based evaporative stress index (ESI)

The Evaporative Stress Index (ESI) is based on a normalized ET metric; namely, the ratio of actual ET to a reference ET (ET_{ref}) expected under non-moisture limiting conditions:

$$f_{RET} = \frac{ET}{ET_{ref}} \tag{4}$$

Scaling actual ET by reference ET aims to focus the index on the soil moisture signal and minimize impacts due to seasonal variations in available energy. In this study, actual ET is retrieved at the ALEXI, MODIS, and Landsat pixel scale using the ALEXI/DisALEXI algorithm, while ET_{ref} is calculated from the FAO-56 Penman-Monteith reference ET for grass, as described in Allen et al. (1998).

ESI is typically computed as standardized anomalies in f_{RET} relative to baseline conditions (Anderson et al. 2007b, 2011, 2013). First, f_{RET} is composited over a moving time window (typically 2, 4, 8 or 12 weeks, depending on the drought timescale of interest), advancing at a 7-day interval. Then ESI is computed as

$$ESI(d,y,i,j) = \frac{\langle v(d,y,i,j) \rangle - \frac{1}{n}\sum_{k=1}^{k=n} \langle v(d,y_k,i,j) \rangle}{\sigma(d,i,j)} \tag{5}$$

where $\langle v(d,y,i,j) \rangle$ is the f_{RET} composite for day d, year y, and i, j grid location, $v(d,y,i,j)$ is the value on day d, n is the number of years in the period of record used to establish the baseline, and $\sigma(d,i,j)$ is the standard deviation in v for that compositing interval. The anomaly space highlights the difference in moisture conditions between years with respect to a multiyear average determined over some period of record. While Yang et al. (2018) used a non-standardized anomaly in the previous 4-year analysis at Mead, NE, due to small sample size, expansion to 8 years in the current study enabled reasonable assessment of the standard deviation term in Eq. (5).

ALEXI ESI is currently computed routinely at 4-km resolution over the continental United States (CONUS) and at 5-km resolution globally and has been used in drought monitoring at regional and global scales. The coarse resolution of the regional product represents a mixture of crops and landcovers with different phenological cycles, limiting its utility for finer scale studies.

3.4. Crop-specific, phenology-corrected ESI

Differences in yield response to water stress occurring at different stages of crop development have been well studied, with reproductive phases often being most sensitive (Wilson 1968; Claassen and Shaw 1970; Cakir 2004). Our hypothesis is that alignment of f_{RET} annual timeseries by crop-specific phenological stage prior to anomaly computation will improve correlations between ESI and yield. Yang et al. (2018) demonstrated the value added in aligning f_{RET} timeseries by emergence date. Here, we further study effects of within-season alignment of stress signals by growth stage, by replacing the calendar-day time axis used in standard ESI computations with a GDD timescale.

A 30-m resolution crop mask (Crop Data Layer; NASS CDL, 2010-2017) for each year was applied to each f_{RET} datacube to identify pixels associated with specific crop types. These identified pixels were then aggregated using linear averaging to the county level. In addition, a generic definition of the day-of-year index, d_p was introduced into Eq. 7 in order to account for year-to-year variability in crop phenology within the ESI computation:

$$ESI(d_p,y,c,u) = \frac{\langle v(d_p,y,c,u) \rangle - \frac{1}{n}\sum_{k=1}^{k=n} \langle v(d_{pk},y_k,c,u) \rangle}{\sigma(d_p,c,u)} \tag{6}$$

where c is crop type (i.e., corn or soybean); u is the unit of spatial aggregation, (i.e., county scale); and d_p is a daily index, which may include a potential temporal shift to accommodate variable emergence date, and may also represent time increments in calendar days or growing degree days.

We applied Eq. (8) to the three study sites at the county level for corn and soybean and evaluated three definitions of d_p: calendar date, emergence-corrected calendar date, and emergence-corrected growing degree days. In the case of the calendar date alignment, d_p was defined as day of year (DOY), starting from January 1st. In the case of emergence-corrected calendar date alignment, d_p was set using the first year in the timeseries (2010) as a baseline and, prior to anomaly computation, time series for other years were adjusted forward or backward based on the difference in that year's crop emergence date relative to emergence in 2010. In the case of growing degree day alignment, d_p reflects growing degree days accumulated from emergence.

3.5. Growing degree day calculation

The rate of crop development through the growing season depends largely on the accumulation of heat (Gilmore and Rogers 1958). The Growing Degree Day, or GDD, is a heat index that has been widely used to assess crop development (Liu et al. 2016; Neild and Newman 1987; Qian et al. 2019). GDD is calculated by subtracting a base temperature from the daily mean temperature, as defined in Eq. (9):

$$GDD = \frac{T_{max} + T_{min}}{2} - T_{base} \tag{7}$$

where T_{max} and T_{min} are daily maximum and minimum air temperatures respectively, and T_{base} is the base temperature under which no significant crop development is expected. T_{base} varies with plant species and $10^{\circ}\ C$ typically is used as the base temperature for corn and soybean crops (Pedersen et al. 2004; Ritchie et al. 1997).

Accumulated GDD on day i ($AGDD_i$) is derived by summing daily GDD (Eq. 10) from a specified starting date as

$$AGDD_i = \sum_{k=e}^{k=i} GDD_k \tag{8}$$

Here we define the beginning accumulation date as the date of corn and soybean emergence (i.e., $k = e$), which will differ due to different planting schedules.

3.6. Yield anomaly – ESI correlation

Over the past several decades, yields of corn and soybean have steadily increased due to technological advances in cultivation and management and genetic improvements in cultivars (Duvick 2005; Egli 2008; Kucharik and Ramankutty 2005). In assessing correlations with climate factors, which typically have shorter-term variability, these longer term yield trends are often removed prior to analysis (Lu et al., 2017). Here, we compute yield anomaly as departures from a linear regression in time over the 2010–2017 period:

$$yield\ (u,y)^{'} = yield(u,y) - yield_{lin}(u,y) \tag{9}$$

where u is the spatial aggregation unit (i.e., county), y is the year, and $yield_{lin}$ is given by a linear temporal fit to all yield data for that unit over the period of record.

To quantify temporal relationships between yield anomalies and ESI, the Pearson correlation coefficient was computed as a function of ESI composite date. Correlations were computed for each modeling domain based on $n_p = n_u \times n_y$ ESI - yield anomaly points, where n_u is the number of counties used in the study domain and n_y is the number of years in the analysis. The peak in the domain correlation curve pinpoints the date of maximum predictive power for yield estimation, and the regression equation derived for that peak date is used for yield estimation (Sec. 3.7). Yield anomaly – ESI correlations were computed for calendar date alignment, emergence-corrected calendar date alignment, and GDD alignment (Sec. 3.4), and improvements in performance due to phenological corrections were assessed in terms of the impact on the peak correlation.

3.7. Yield estimation and evaluation

The predictive power of within-season ESI for estimating at-harvest, county-level yield was assessed using a bootstrapping strategy that was applied in both the time and space domains. Two tests were performed to assemble the $n_p = n_u \times n_y$ samples used to generate regression equations used for yield estimation, leaving out one year and one county in the bootstrapping analysis. The leave-one-year-out test evaluates the temporal (inter-annual) predictive capability of the ESI-yield relationship, while the leave-one-county-out test assesses capacity for spatial extrapolation. Regression equations between yield anomalies and ESI were derived from the remaining samples and applied to the year or the county excluded from bootstrapping. Lastly, the yield estimates and yield anomalies were compared with NASS county-level yield data. Yield estimation and evaluation were conducted for the calendar date, emergence-corrected calendar date, and GDD temporal alignments.

4. Data

4.1. Micrometeorological measurements

All three of the study domains contained two or more eddy covariance systems collecting measurements of solar radiation (Rs), net radiation (Rn), latent heat (λE), sensible heat (H), soil heat flux (G) and momentum fluxes, as well as temperature, wind speed and direction, humidity and precipitation. Seven flux towers were used in this study to evaluate the accuracy of the 30-m daily ET retrievals (Table 1). Flux towers USNe1, USNe2, and USNe3 (PI: A. Suyker) are located within the University of Nebraska Agricultural Research and Development Center near Mead, NE. Fields USNe1 (48.7 ha) and USNe2 (52.4 ha) are irrigated (center pivot), whereas field USNe3 (65.4 ha) is rain-fed (Suyker et al. 2004). Three AmeriFlux towers (USBr1, USBr2 and USBr3; PI: J. Prueger) operate within the Ames, IA domain. The footprints of USBr1 and USBr3 sample two adjacent fields, whereas USBr2 was installed on the common boundary of these fields and may be influenced by both, depending upon the wind direction. In this study, only USBr1 and USBr3 have been used. The Champaign site has hosted a long-term AmeriFlux flux tower installation (USBo1, PI: T. Meyers) since 1996 (Meyers and Hollinger 2004). USBo1 is in a rain-fed field, cultivated with alternating years of soybean and corn crops. In addition, the University of Illinois-Champaign maintains several flux towers in this area including USUiC which was installed in a rainfed corn/soybean rotation field (PI: C. Bernacchi).

Due to the fact that the eddy covariance flux measurement technique does not enforce energy closure, we assessed model-observation agreement using both observed fluxes and fluxes forced with a “residual correction” approach, which assigns the entire residual of the observed energy budget at the daily timescale to the daily latent heat flux ($\lambda E\ closed = RN - H - G$) (Prueger and Kustas, 2005). The observed and residual closure values likely bound the true latent heat flux, and associated model errors. Average closure errors ($\lambda E\ closed - \lambda E$) were 16–29% of daily net radiation for the towers and time periods listed in Table 1. For details regarding the flux and supporting micrometeorological measurements at Mead, Ames, and Champaign, readers are referred to Suyker and Verma (2009), Hatfield et al. (1999), and Meyers and Hollinger (2004).

4.2. NASS yield and crop progress data

The USDA National Agricultural Statistics Service (NASS) produces monthly yield forecasts for the major commodities during the second half of the growing season at U.S. national and state levels. These estimates are primarily based on data collected through two surveys: Agricultural Yield (AY) and Objective Yield (OY) (NASS/USDA, 2006). The AY is a phone-based survey sampling thousands of producers across the country, asking them about perceived crop yields from their farm. The OY on the other hand is a plot-based survey in which very small within-field areas are randomly sampled and visited by an enumerator to obtain biophysical measurements for ascertaining yields. Given the OY is much more labor intensive, the sample size is only in the hundreds and limited to intensive growing states and major commodities. It should also be noted that within the last few years, remote sensing

Table 1
Flux tower data collected at Mead, Champaign, and Ames sites for validation.

Site	State	Tower	Lat	Long	Years	Dominant land cover
Mead	NE	USNe1	41.165	−96.477	2010–2017	irrigated corn/soybean field
Mead	NE	USNe2	41.165	−96.470	2010–2017	irrigated corn/soybean field
Mead	NE	USNe3	41.180	−96.440	2010–2017	rainfed corn/soybean field
Ames	IA	USBr1	41.976	−93.693	2010–2017	rainfed corn/soybean field
Ames	IA	USBr3	41.974	−93.694	2010–2017	rainfed corn/soybean field
Champaign	IL	USBo1	40.052	88.373	2010–2016	rainfed corn/soybean field
Champaign	IL	USUiC	40.063	−88.196	2010–2016	rainfed corn/soybean field

information from MODIS has also been adding independent and ancillary information to better affirm the results of both the AY and OY surveys.

For corn and soybeans, the first seasonal yield estimates are based on August 1 conditions and published no later than the 12th of the same month. Updated forecasts are then produced with the same day of month constraints for September, October and November. After harvest is fully complete, the finalized national and state yield estimates are released in January of the next year in the NASS Annual Summary report. Next, county-level estimates are released in late February based on a yet another survey, this time mail-based and having occurred in the late fall. The county efforts are different in that they are not probability-based, asking for crop statistics beyond just yield, and managed independently for each state. However, the data ultimately reconcile to the Annual Summary established state yields and thus do not exist in isolation. Note that NASS does not publish measures of uncertainties alongside its county average estimates, given the complicated mix of survey and model information being integrated.

NASS also publishes weekly state-level Crop Progress (CP) and Condition reports giving estimates of crop development stage for primary crops. These span planting to harvest from April to November. While the data collected for these reports are qualitative in that they rely on the expert judgement of local cooperative crop reporting respondents within each sampled state, they show reasonable agreement with remotely sensed phenological metrics (Gao et al., 2017, 2020). Progress data for corn are expressed as a percentage of the crops in the reporting unit (state level for publically available data) planted, emerged, silking, doughing, dented, mature, and harvested; and for soybean as a percentage of the crop planted, emerged, blooming, setting pods, dropping leaves, and harvested. The average number of days reported by NASS from 20 to 80% emergence for the study states and period was 16 days for corn and 19 days for soybean. In specifying annual phenological offsets for each county we define "emergence date" as the midpoint of this range – the day a crop achieved about 50% emergence within that state.

4.3. Growing degree day (GDD)

Growing Degree Day data for corn were obtained from the High Plains Regional Climate Center (HPRCC) Corn Growing Degree Day (GDD) decision support tool (https://hprcc.unl.edu/gdd.php), which provides high quality data that are widely used for crop development analysis in the Midwest (Skaggs and Irmak 2012; Grassini et al. 2015). The HPRCC-accumulated corn GDD for counties starts from the earliest insurable planting dates for corn (by county) based on the 2014 crop insurance records or from April 1 if there is no crop insurance record available. Because there are no soybean GDD data readily available, in this study, we calculated the accumulated soybean GDD from the HRPCC corn GDD by adjusting the starting date. Specifically, we recalculated the accumulated GDD from daily GDD starting from the state-level crop emergence date obtained from the NASS CP reports for corn and soybean (NASS CP, 2010-2017).

4.4. ET model inputs

ALEXI is routinely run over the CONUS at 4-km resolution using brightness temperature observations from the Geostationary Operational Environmental Satellites (GOES). Land-surface temperature data retrieved from GOES-East (at 75°W) and GOES-West (at 105°W) are combined to provide a full coverage of CONUS (Anderson et al. 2007a, 2007b).

ALEXI 4-km ET fields were disaggregated to 500 m resolution using standard Collection 6 MODIS products as input to the DisALEXI algorithm. These include LST and view angle maps (MOD11_L2; Wan et al. 2015), geolocation fields (MOD03), land-surface albedo (MCD43A; Wang et al. 2018) and leaf area index (LAI) (MCD15A3H; Myneni, et al. 2015). A gap-filling and smoothing technique was applied to the MODIS ET retrievals to obtain daily data and fill gaps due to clouds and swath limitations (Yang et al. 2018).

Periodic ET retrievals at 30-m resolution were also obtained with DisALEXI using Landsat data over three Worldwide Reference System (WRS) scenes: Mead (path 28/row 31), Ames (path 26/row 31), and Champaign (path 23/row 32). Landsat 5, 7, and 8 data from 2010 to 2017 were acquired for these path-row scenes. A total of 330, 142, and 214 Landsat scenes were processed for Mead, Ames, and Champaign, respectively, excluding any scenes with snow cover or > 30% cloud cover. The resulting average Landsat revisit frequency was 15 days between images, with a maximum gap of 33 days in the growing season from April to October.

Atmospherically corrected Landsat surface reflectance (SR) data at 30-m resolution were downloaded from the USGS Earth Resources Observation and Science (EROS) Center. TIR data at were also downloaded and were atmospherically corrected using MODTRAN (Berk et al. 1989; Cook et al. 2014). Because the TIR data have varying native spatial resolution (120 m, 60 m and 100 m for Landsats 5, 7, and 8, respectively), the Data Mining Sharpener (DMS; Gao et al. 2012a) tool employing a TIR-SR machine learning technique was applied to the thermal data to achieve a consistent 30-m resolution for all Landsat scenes. LAI at 30-m resolution was derived from MODIS 500-m LAI and Landsat 30-m SR data using a reference-based regression tree approach (Gao et al. 2012b). Gaps in derived Landsat ET images due to cloud cover or scan line corrector failure (Landsat 7) were filled using the gap-filling technique described by Yang et al. (2017).

For both ALEXI and DisALEXI, meteorological model inputs of solar radiation, wind speed, air temperature, vapor pressure, and atmospheric pressure were obtained from the Climate Forecast System Reanalysis (CFSR; Saha et al. 2014) archive.

5. Results

5.1. Model evaluation with flux observations

To test the performance of the DisALEXI-Landsat retrievals, which provide the high-resolution spatial structure for the fused daily ET timeseries, the modeled energy balance was compared with daytime-integrated measurements from the seven flux towers. Model fluxes of daily solar radiation, net radiation, latent heat, sensible heat, and soil heat on the Landsat overpass dates during the growing season (DOY 90–300) were extracted from DisALEXI-Landsat output at the tower locations. Fluxes were averaged over a box of 3 by 3 Landsat pixels around the tower locations to represent the surface footprint with a dimension on the order of 100 m. For some flux tower sites (e.g. USBo1), the extraction point was offset by 1–2 Landsat pixels to avoid field edge effects.

The statistical accuracy of the model flux partitioning on Landsat dates over the seven flux tower sites (Table 1) is presented in Fig. 3 and reported in Table 2. Quantitative measures include the number of observations, the mean observed flux, the mean modeled flux, the mean bias error (MBE), the mean absolute error (MAE), the root mean square error (RMSE), and the percent error (% ERR, defined as the ratio of MAE and the mean observed flux).

Across the three study sites, the primary energy inputs – solar radiation (Rs) and net radiation (Rn) - agree reasonably well with local measurements. Solar radiation from CFSR has errors on the order of 5% at the seven flux sites, while errors in net radiation are on the order of 10%. Errors in Rs are comparable to insolation accuracies reported at other study sites (Anderson et al. 2019), with a few outliers where cloud conditions were not well represented in the CFSR reanalysis. In future studies, geostationary satellite-derived insolation products could be used to improve model radiation input (Anderson et al. 2019).

Modeled latent heat fluxes are compared to observations both with and without closure correction, which generally can be considered to

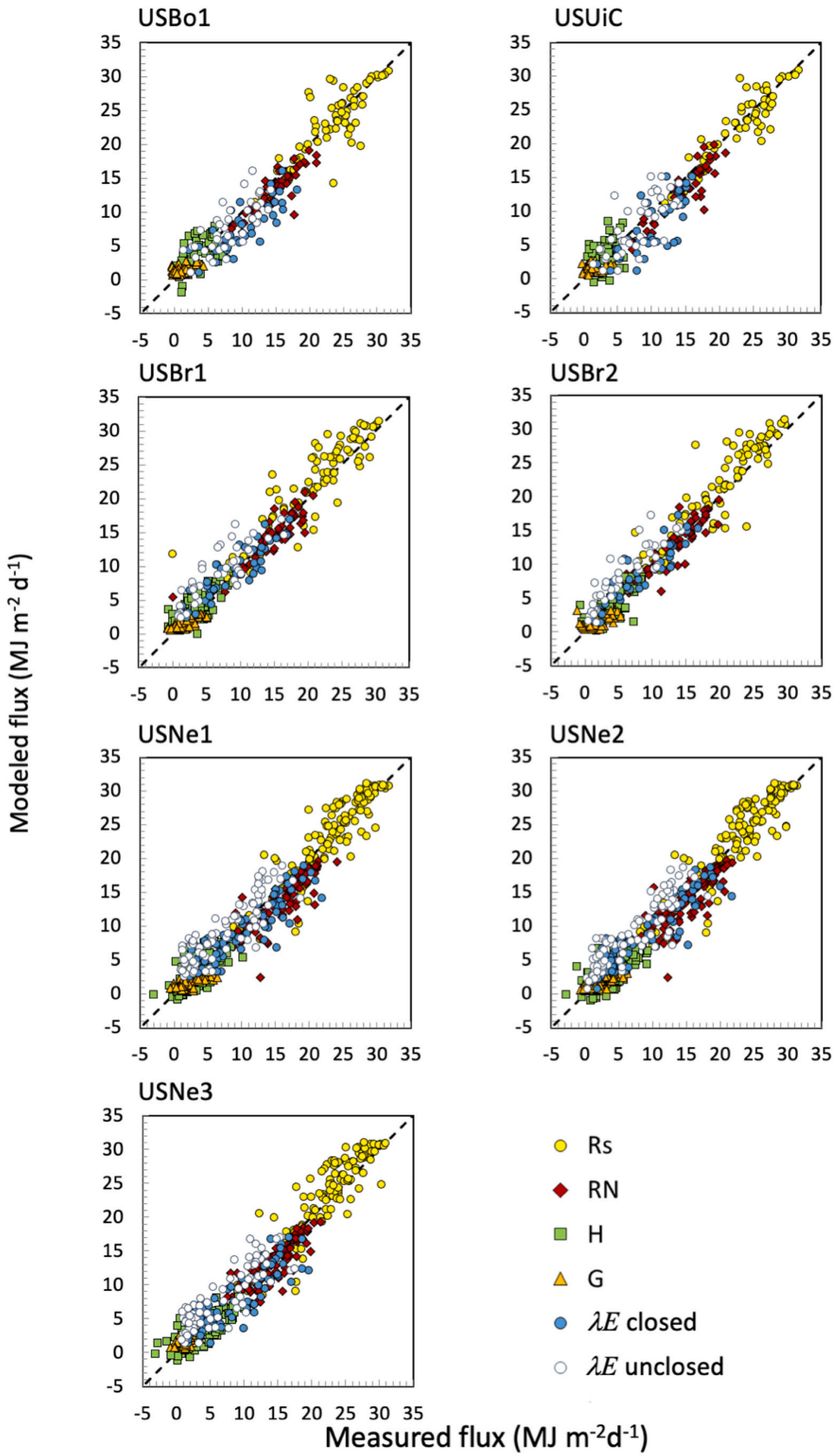

Fig. 3. Comparisons of observed and Landsat-retrieved daytime integrated fluxes on Landsat overpass dates at the seven flux tower sites within the three modeling domains: USBo1 and USUiC (Champaign); USBr1 and USBr3 (Ames); USNe1, USNe2, and USNe3 (Mead).

Table 2
Summary of the statistical indices quantifying model performance for daytime-integrated surface energy fluxes on Landsat overpass dates at the seven flux tower stations (unit: $MJm^{-2}\ d^{-1}$), and daily ET from the fused timeseries (unit: mm d^{-1}).

Flux tower	Stats	Rs	Rn	H	G	λE unclosed	λE closed	Daily ET unclosed	Daily ET closed
USNe1	N	68	68	68	68	68	68	1412	1412
	Mean O	25.2	16.7	2.3	3.5	8.3	11.0	2.8	3.8
	Mean P	25.2	14.6	1.6	3.2	9.8	9.8	3.4	3.4
	RMSE	2.0	2.6	1.3	1.9	2.8	2.7	1.3	1.2
	MBE	0.0	−2.1	−0.7	−0.3	1.5	−1.1	0.7	−0.4
	MAE	1.4	2.2	0.9	1.5	2.4	2.0	1.1	0.9
	% error	5.4	12.9	39.8	43.0	29.3	17.8	38.3	24.2
USNe2	N	72	72	72	72	72	72	1565	1565
	Mean O	25.1	16.0	2.2	3.6	8.4	10.2	2.7	3.4
	Mean P	25.2	14.5	1.6	3.1	9.7	9.7	3.3	3.3
	RMSE	2.0	2.1	1.2	2.0	2.9	2.5	1.3	1.2
	MBE	0.1	−1.4	−0.6	−0.4	1.3	−0.5	0.5	−0.1
	MAE	1.3	1.6	0.9	1.5	2.4	1.8	1.0	0.9
	% error	5.3	9.9	41.4	43.2	29.1	17.2	38.3	25.8
USNe3	N	65	65	65	65	65	65	1395	1395
	Mean O	24.0	14.9	1.6	4.3	7.2	9.1	2.4	3.1
	Mean P	24.7	13.6	1.7	3.7	8.1	8.1	2.9	2.9
	RMSE	2.1	2.0	0.8	2.2	2.6	2.8	1.2	1.1
	MBE	0.7	−1.3	0.2	−0.5	1.0	−1.0	0.5	−0.3
	MAE	1.5	1.5	0.6	1.9	2.2	2.2	0.9	0.9
	% error	6.1	9.8	41.3	44.9	30.8	24.0	37.9	26.9
USBr1	N	32	32	32	32	32	32	1103	1103
	Mean O	24.1	15.8	2.1	3.9	7.7	9.8	2.4	3.2
	Mean P	25.7	15.4	1.6	4.2	10.0	10.0	3.3	3.3
	RMSE	2.5	1.7	1.0	1.9	3.3	2.3	1.4	1.1
	MBE	1.6	−0.4	−0.5	0.4	2.3	0.1	0.8	0.0
	MAE	2.1	1.3	0.8	1.6	2.7	2.0	1.1	0.9
	% error	8.7	8.5	38.4	41.3	35.1	20.0	45.4	26.6
USBr3	N	32	32	32	32	32	32	1188	1188
	Mean O	22.9	14.2	1.9	3.8	6.8	8.5	2.3	3.0
	Mean P	24.5	14.2	1.6	4.2	8.9	8.9	3.2	3.2
	RMSE	2.2	1.6	1.3	1.9	3.1	2.1	1.5	1.1
	MBE	1.6	0.0	−0.3	0.3	2.1	0.4	0.9	0.2
	MAE	1.8	1.2	0.9	1.4	2.5	1.7	1.2	0.9
	% error	7.8	8.2	49.5	37.2	37.2	19.4	51.5	28.7
USBo1	N	35	35	35	35	35	35	777	777
	Mean O	24.3	14.7	2.5	3.8	7.8	8.4	2.7	3.0
	Mean P	24.5	14.4	1.6	3.7	9.0	9.0	3.4	3.4
	RMSE	2.2	1.8	2.1	2.0	2.8	2.7	1.4	1.3
	MBE	0.2	−0.3	−0.9	−0.2	1.2	0.6	0.7	0.4
	MAE	1.2	1.2	1.6	1.6	2.2	2.1	1.1	1.0
	% error	5.0	8.4	64.4	41.9	27.5	25.5	40.7	34.2
USUiC	N	33	33	33	33	33	33	852	852
	Mean O	25.1	15.9	3.1	1.4	9.4	11.4	3.3	3.7
	Mean P	24.5	14.3	3.8	1.6	8.9	8.9	3.2	3.2
	RMSE	1.2	2.1	2.3	1.1	3.1	3.7	1.4	1.4
	MBE	−0.6	−1.6	0.7	0.2	−0.5	−2.5	−0.1	−0.5
	MAE	1.1	1.8	1.9	0.9	2.6	3.0	1.1	1.1
	% error	4.4	11.6	63.0	61.7	27.3	26.2	33.9	28.5
All sites	N	337	337	337	337	337	337	8292	8292
	Mean O	24.4	15.4	2.2	3.5	7.9	9.8	2.7	3.3
	Mean P	24.9	14.4	1.9	3.4	9.2	9.2	3.2	3.2
	RMSE	2.0	2.0	1.4	1.8	3.0	2.7	1.3	1.2
	MBE	0.5	−1.0	−0.3	−0.1	1.3	−0.6	0.6	−0.1
	MAE	1.5	1.5	1.1	1.5	2.4	2.1	1.1	0.9
	% error	6.1	10.0	49.7	43.1	30.6	21.4	40.2	27.7

N: number of samples; Mean O: mean observed flux; Mean P: mean predicted flux; RMSE: root mean square error; MBE: mean bias error; MAE: mean absolute error; Rs: solar radiation; Rn: net radiation; G: soil heat flux; H: sensible heat flux; λE: latent heat flux; ET: evapotranspiration. The closed values indicate that the energy balance residual correction has been applied (Prueger and Kustas, 2000), while unclosed indicates that energy balance closure was not imposed on the measurements.

bound the 'true' flux. The 'residual corrected' latent heat flux has better agreement in the three study sites, as might be expected since the TSEB inherently closes the modeled energy budget. Differences between modeled and observed fluxes reflect a combination of both model and observational error, including errors from imposing energy balance closure. Percent errors on Landsat overpass dates are on the order of 17–25%, consistent with typical errors of 20% or larger obtained in previous flux measurement comparison studies (Kustas and Norman, 1997; Twine et al. 2000; Wilson et al. 2002).

The fused daily ET estimates show good agreement with ET measurements computed from the closed latent heat flux values (last column in Table 2), with RMSE of 1.1–1.3 mm d^{-1} and MAE of 0.9–1.1 mm d^{-1} for all flux sites. These daily ET accuracies are close to the performance reported from prior ET fusion experiments (Cammalleri et al. 2013, 2014; Semmens et al. 2016; Sun et al., 2017; Yang et al., 2017) and are in line with the target model accuracy of approximately 1 mm d^{-1} for agricultural applications as cited by Seguin et al. (1999).

Fig. 4 compares modeled fused daily ET with time-series observations from the seven flux towers across the Mead, Ames, and Champaign study sites. Note that 2015 ET observations from the USNe3 flux site are

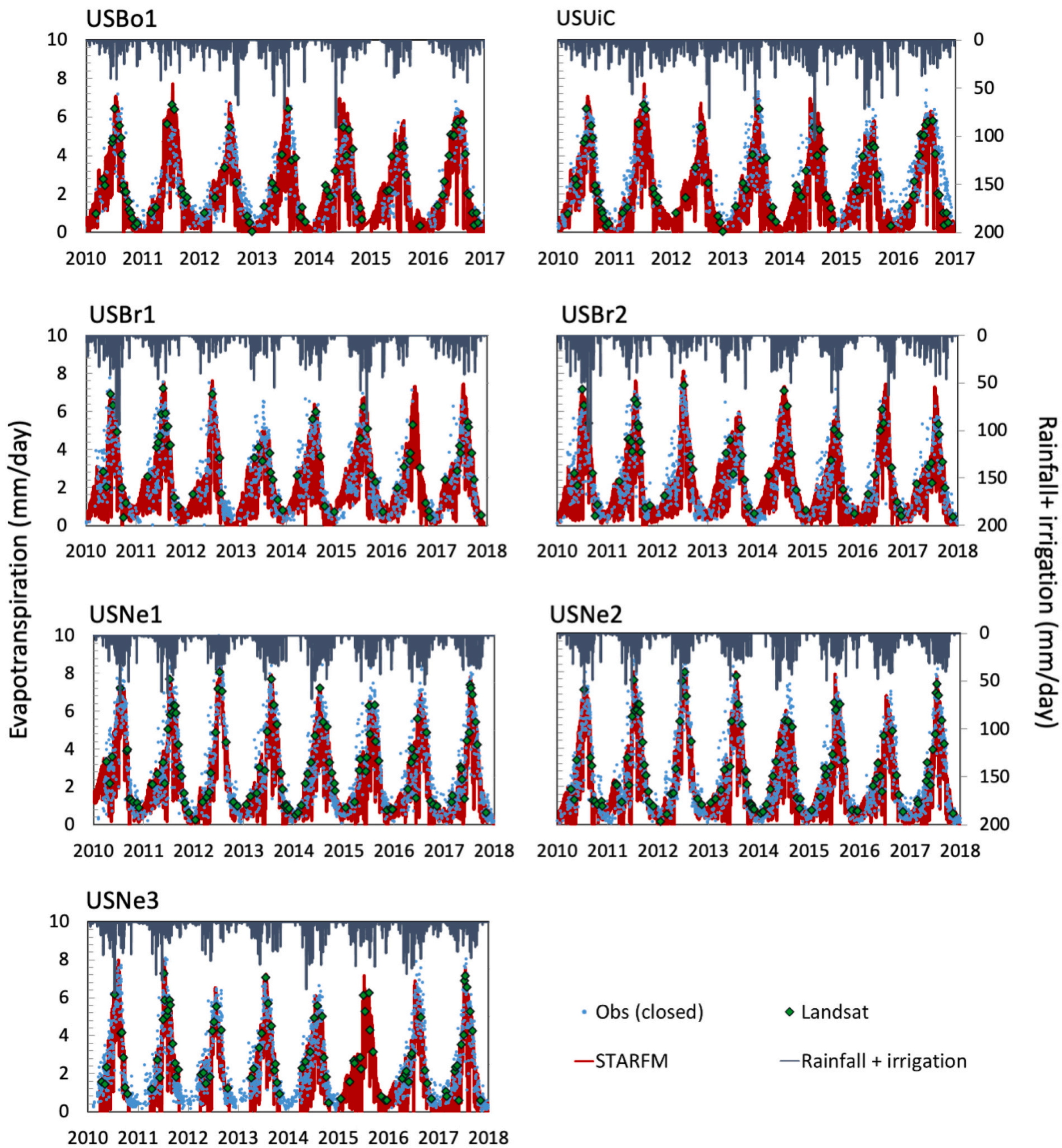

Fig. 4. Timeseries of closed ET observations (blue dots), 30-m ET retrievals on Landsat overpass dates (green diamonds), and daily ET estimates from STARFM (red line) at the seven flux tower sites. Precipitation is shown on the top of each panel as dark blue bars. Mead includes USNe1, USNe2, and USNe3 flux towers; Ames includes USBr1, and USBr3; Champaign includes USBo1 and USUiC. Note that USNe1 and USNe2 are located in irrigated fields, and therefore the precipitation amount includes both rainfall and irrigation. The other five tower sites are in rain-fed fields. (For interpretation of the references to colour in this figure legend, the reader is referred to the web version of this article.)

not included in the comparison due to data availability issues. In general, the fused ET estimates reproduce the observed seasonal and interannual trends at the seven flux towers. In some sites and years, however, the model missed the peak value in the observed ET (e.g., USBr1 in 2013, USUiC in 2013 and 2016). In these cases, no clear Landsat scenes were available during the peak ET period due to cloud cover and the fused timeseries were not able to recover the highest fluxes.

5.2. Yield and phenology variations

Before analyzing yield-ESI correlations, we examined the natural variability in yield, emergence date, and forcing meteorological conditions that occurred over the period of record. Fig. 5a shows annual mean corn and soybean yields for counties in the three study domains, along with box plots that show yield averages and variability for each site over the full study period. These box plots demonstrate an increase in both corn and soybean yield and yield variability from west to east (i.e., from Mead, NE to Champaign, IL). The lowest yields occurred in the 2012 flash drought year, except for soybean at Ames.

The higher yield variability at Ames and Champaign, particularly for corn, may be related to variability in annual rainfall (Fig. 5b) given that most crops in these regions are rain-fed. The USDM plots (Fig. 2) indicate that the Mead domain was most impacted by drought over the study

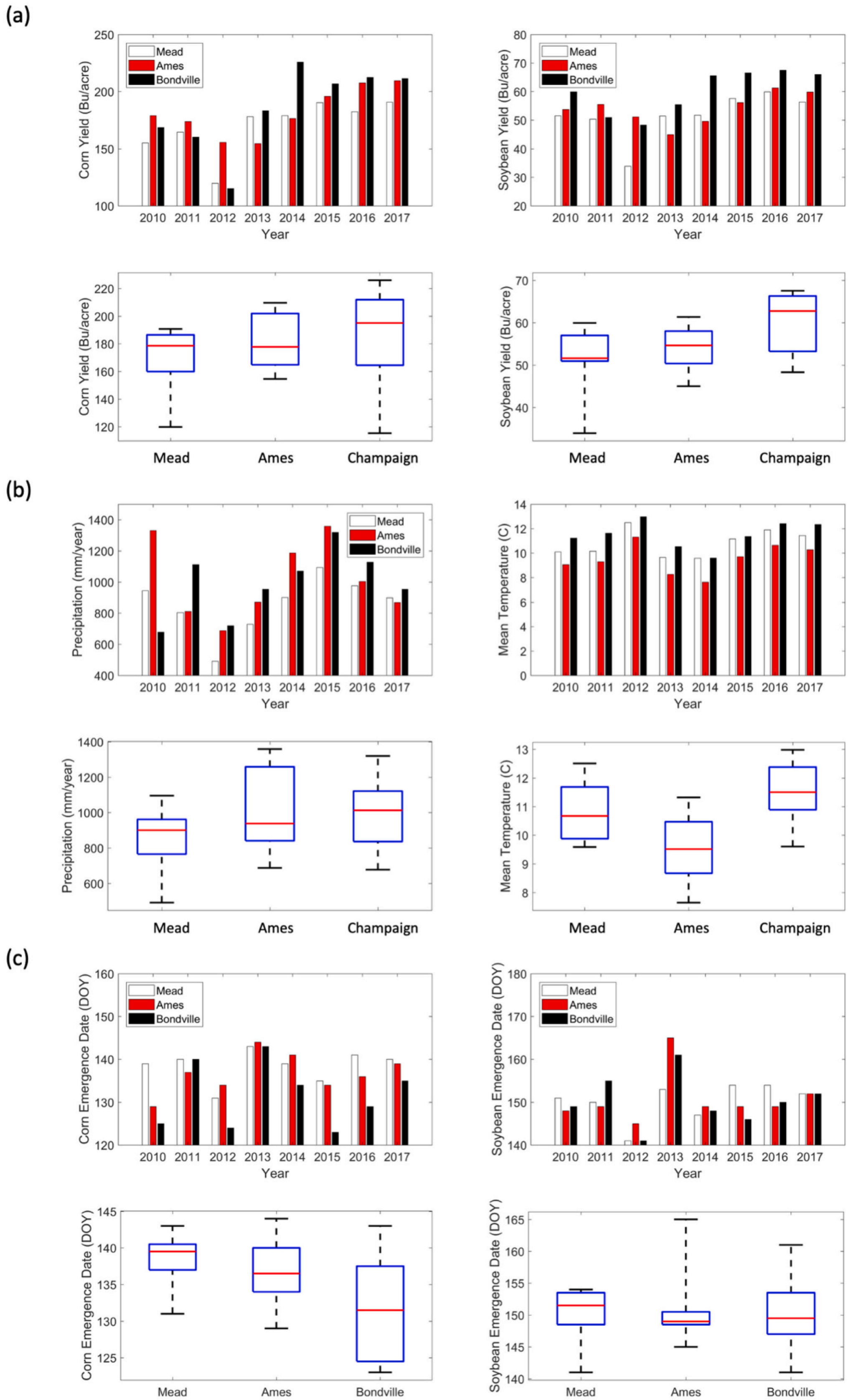

Fig. 5. Yield (a) precipitation and temperature (b) and emergence date (c) variation across Mead, Ames, and Champaign for corn and soybeans (2010–2017). Boxes are drawn from 25th percentile to 75th percentile of the data with a horizontal red line denoting the median. Whiskers represent the minimum and maximum data value. Data source: USDA NASS county level yield; DAYMET 1 km data; USDA NASS state level crop progress reports. (For interpretation of the references to colour in this figure legend, the reader is referred to the web version of this article.)

period. Temperature values show similar levels of year-to-year variability across the three study sites, with cooler temperatures at Ames due to its higher latitude.

Mean emergence date also varied across the three study sites, with a tendency toward later emergence for both corn and soybeans from west to east. The earliest corn emergence date at the Mead site occurred in 2012, due to higher early season temperatures and growing degree day accumulation. The latest soybean emergence date at Ames was in 2013, with extreme wet conditions in early spring delaying planting, and therefore emergence. These conditions also contributed to the low soybean yields in that year. In summary, the combined study domain exhibited notable variability in phenology, yield and climate conditions over the period of record, warranting evaluation of phenological corrections to the ESI-yield relationships.

5.3. Correlations between yield anomalies and ESI at county level

Fig. 6 shows the correlations between yield anomalies and ESI for the three time-axis alignments (calendar date, emergence date, and accumulated GDD) for corn and soybeans, for individual counties (colored curves) and for all counties within the domain combined (black dashed curve). The vertical solid lines indicate average emergence date and harvest date as obtained from NASS CP reports. While the calendar date and emergence date alignment plots cover the growing season (week 15 to week 45), the GDD plot shows the period starting from emergence and ending at 3000 AGDD which is beyond physiological maturity for both corn and soybeans. The vertical dashed line indicates the date when USDA NASS releases the first yield estimates for corn and soybeans (August 1). In the GDD plot, this line represents the average AGDD on August 1 over the period of record to allow for comparison with the calendar date alignment.

The temporal correlation patterns between emergence and harvest are qualitatively similar between the three alignments. In many, but not all, cases, the emergence-corrected and GDD alignments have the advantage of reducing noise in the correlation curve. One notable feature is that the GDD alignment shifts the peak correlation to an earlier date than that obtained with the calendar and emergence-corrected alignment. The GDD alignment also tends to broaden and smooth the period of peak correlation, which confirms its value in controlling for variable growth rate post emergence. Patterns in GDD-aligned correlation curves are strikingly similar between the corn and soybean crops.

For all three time-axis alignments for corn, the peak correlation in the mean curve occurs before the harvest event (right vertical line in Fig. 6), indicating predictive power for within-season yield estimation prior to harvest. Peak correlation pre-harvest for corn fields ranges from 0.67 to 0.98 and occurs 4–16 weeks before harvest. In some cases, the peak correlations are several weeks before August 1, prior to the yield estimate released from USDA NASS. In the GDD alignment, the peak correlations in the mean curve are before August 1st for the three sites and they all fall between 1000 and 1400 AGDD, the accumulated heat required for silking in corn (Neild and Newman, 1990). This coincides with the findings of Yang et al. (2018) that peak correlations between field-scale ESI and yield anomalies at the Mead flux sites occurred 68 days after emergence, corresponding to the silking stage for maize when grain development is particularly sensitive to soil moisture deficiencies.

The peak correlation for soybeans occurs before the harvest event in all three alignments at the three study sites. Peak correlations for soybean fields range from 0.58 to 0.98 and occur 10–15 weeks before harvest. The peak correlations in the GDD alignment fall between 1100 and 1500 AGDD, which is roughly around the initial reproductive stage and before physiological maturity (Pedersen et al., 2004). Studies have shown that in water-limited environments, maximum water use in soybeans occurs during reproductive stages, when the yield is very sensitive to moisture deficiency (Dogan et al. 2007; Pejić et al. 2011). Water stress imposed during reproductive stages (e.g., beginning of pod, beginning of seed, and full seed) can result in a substantial yield reduction compared to a fully watered crop (Dogan et al. 2007; Korte et al. 1983).

In general, the phenology-based alignment of the f_{RET} timeseries prior to anomaly computation improves performance in terms of noise-reduction, timeliness and window of peak correlation. An exception is seen in the case of soybeans within the Ames domain, where both emergence and GDD alignments reduce peak correlation between ESI and yield anomalies. The correlation curve collapses to a narrow peak during the growing season in the calendar date alignment relative to other cases. The emergence and GDD alignments further reduce the peak (from 0.91 to 0.79, and 0.78, respectively), although the window for peak correlation is broadened. This reduction is thought to be due primarily to a large shift in the emergence date in 2013 as revealed in Fig. 5c, where NASS reported a more than two-week delay in soybean emergence at the state level relative to the median 2010-2017 date. This was due to extremely wet conditions during the early spring of 2013 which delayed planting. This delay, however, may be spatially variable across the state and not well-represented at the county scale by the state level reports. This suggests the potential value of integrating timely remotely sensed indicators of crop phenology, as discussed further in Sec. 6.2.

5.4. Yield estimation at county level

The regression functions between yield anomaly and the ESI derived on the peak correlation date (as seen in Fig. 6) can be used for yield estimation. As an independent test of the accuracy of the ESI-based yield and yield anomaly estimates, the “leave-one-out” bootstrapping methods described in Sec 3.8 were applied. Figs. 7 and 8 compare NASS county-level yield data for corn and soybeans with yield estimates generated from the two bootstrapping strategies using calendar date, emergence-corrected calendar date, and GDD temporal alignments. Results for both yield anomalies and yield are shown. Note that the yield anomaly is estimated directly from the regression equations, whereas estimated yield is the sum of estimated yield anomaly and the multi-year yield trend.

Figs. 7-8 show that correlations for yields are higher than for yield anomalies in all cases. This is expected, given that adding back the data-derived yield trends artificially boosts the correlation. In addition, the “leave-one-county-out” bootstrapping strategy produces higher correlations than the “leave-one-year-out” tests, especially for the calendar date and corrected-emergence alignments. While spatial autocorrelation in yield and ESI variability between counties is likely inflating the correlation coefficients in this case, these results were retained as a baseline for assessing the “leave-one-year-out” evaluations.

Using the “leave-one-year-out” bootstrapping strategy, the GDD alignment provides superior yield estimates in comparison to the other two time-axis alignments across all sites and for both crops (Figs. 7-8). The fact that comparable accuracies are achieved with GDD between both bootstrapping strategies suggests that in accounting for the annual variability in growing season conditions we can derive yield relationships using the heat unit scale which are more robust in both time and space.

For example, for the “leave-one-year-out” sampling strategy, corn and soybean yields in the 2012 flash drought year were poorly predicted by regression equations developed from the other years of data with both calendar date and emergence date alignments, particularly for the Mead and Champaign sites (Figs.7–8). The extreme conditions for that year were not well represented among the remaining data under those alignments. However, the use of GDD enabled the low yields in 2012 to be reasonably predicted from relationships in other years.

In most cases, simply correcting for the emergence date improved correlations between ESI and yield anomalies, as found in Yang et al. (2018). A notable exception was seen in the case of soybeans at Ames, where the “leave-one-year-out” correlation between estimated and observe yield anomalies was reduced from 0.32 to 0.17 by aligning f_{RET}

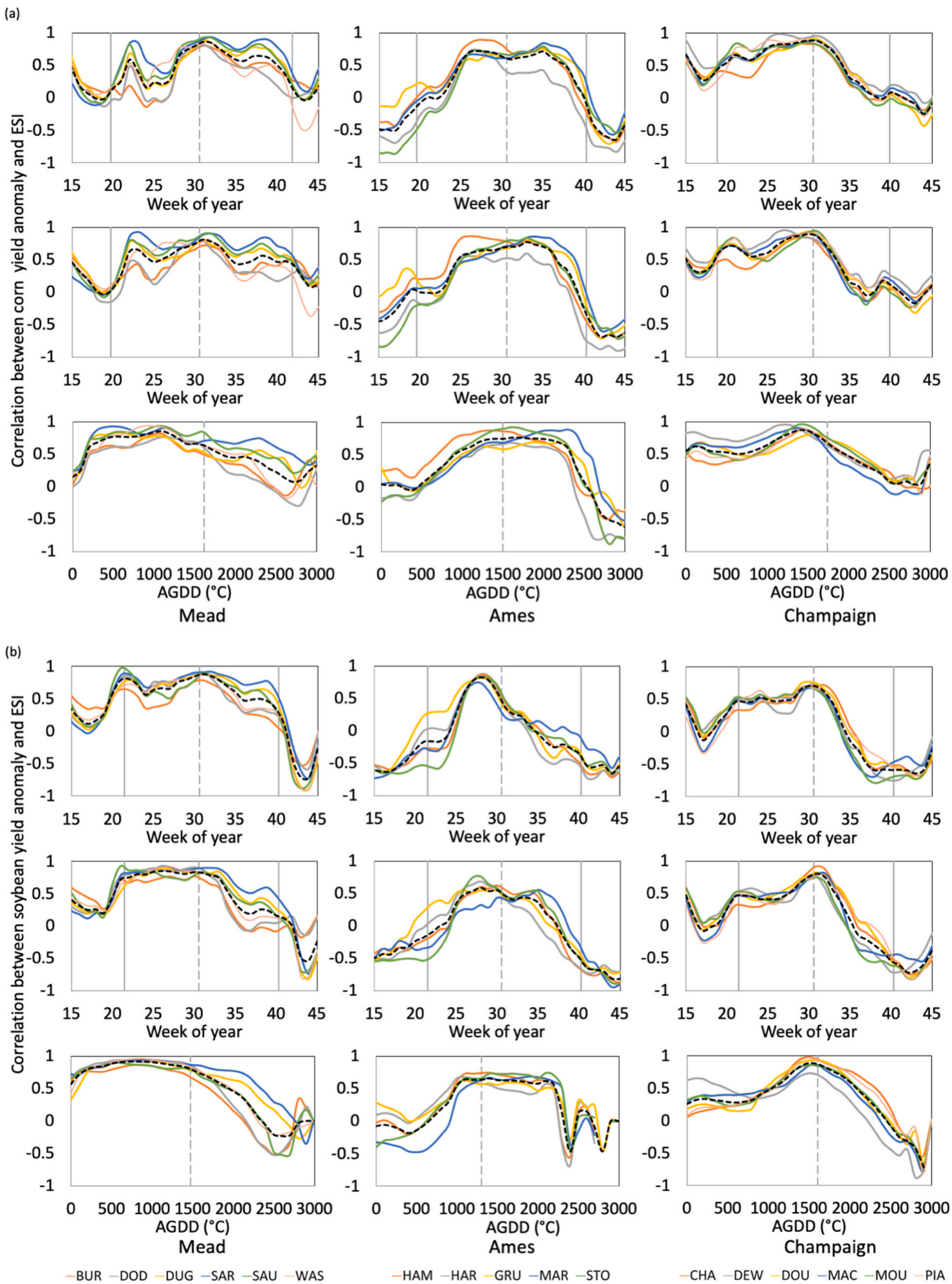

Fig. 6. Correlation between yield anomalies and ESI for corn (a) and soybean (b) as a function of calendar date (top); calendar date with emergence correction using 2010 as baseline (middle); and AGDD (bottom) at Mead (left), Ames (middle) and Champaign (right). Colored curves indicate correlations for individual counties, while the black dashed curve includes all counties within the domain. The vertical solid lines indicate average emergence and harvest dates. The vertical dashed line denotes August 1.

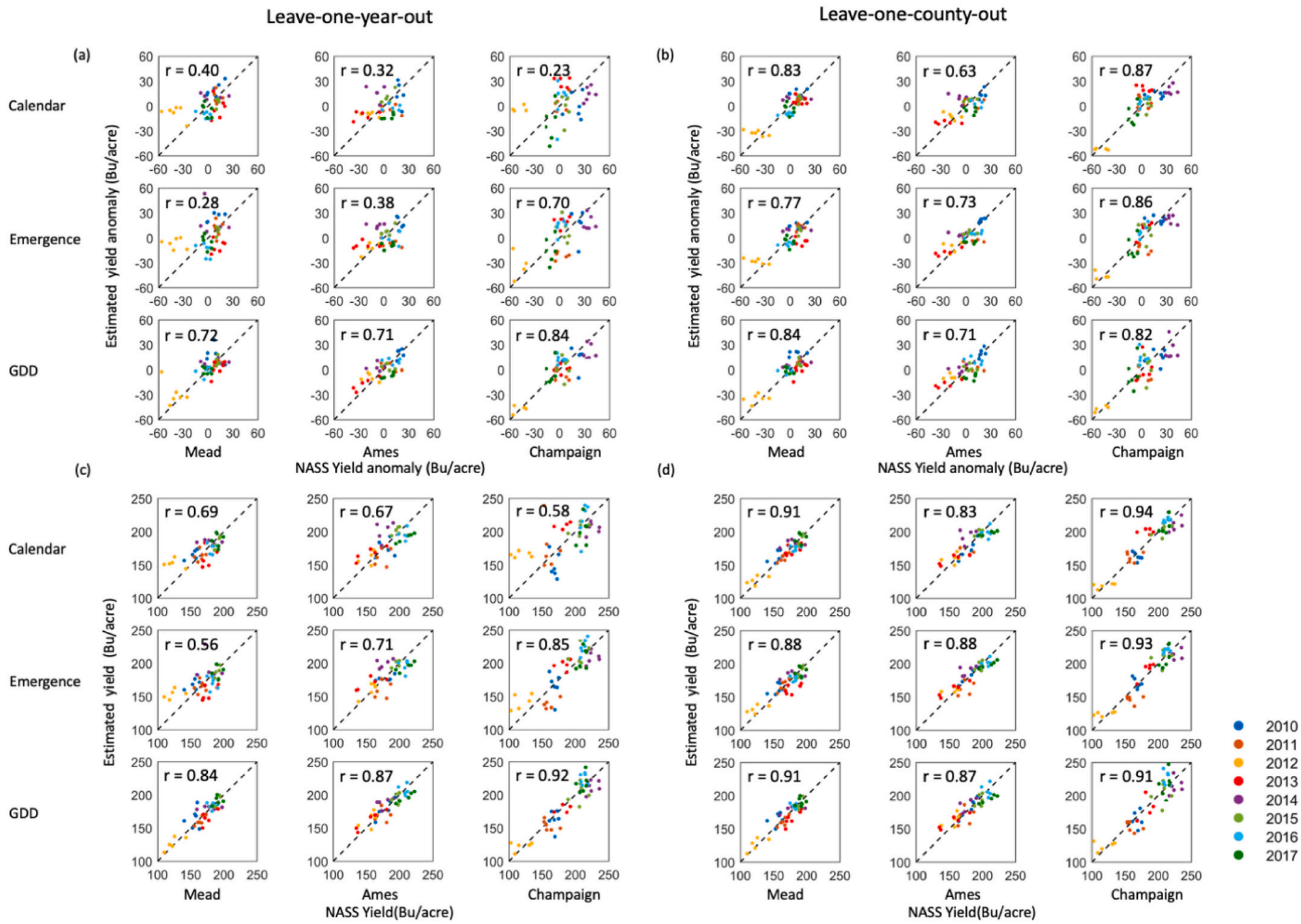

Fig. 7. Comparison of corn yield anomaly (a, b) and yield (c, d) reported by NASS yield and yields estimated using two bootstrapping strategies: leave-one-year-out (left column) and leave-one-county-out (right column). In each plot, there are three alignments: calendar date (top row in each plot); calendar date with emergence correction using 2010 as a baseline (middle row in each plot); and AGDD (bottom row in each plot) for Mead (left), Ames (middle), and Champaign (right) 2010–2017. Each dot is the yield for one county for a given year. The X-axis is the NASS yield survey data and the Y-axis is the modeled yield.

on the emergence date. As noted in Sec. 5.3, this is largely due to the 2013 growing season where the delayed emergence reported at the state level in the NASS crop progress reports may not have been representative of all the counties included in this study. Fig. 8 indicates that the large correction for late soybean emergence at Ames in 2013 had the effect of degrading yield estimates for 2013 and 2014 with the emergence date time-axis alignment. However, with additional modification of the time axis post-emergence, accounting for variability of within season crop progress using GDD time units, correlations for yield anomalies improved from 0.17 to 0.56, comparable to the all-year peak correlations in Fig. 6. A similar result is obtained at Mead where drought impacts on corn yields in 2012 were better captured when annual stress curves were aligned by phenological growth stage using GDD.

These collective results are summarized in Fig. 9, showing RMSE in yield estimates from the two bootstrapping sampling approaches and three time-axis alignments. The leave-one-county-out prediction accuracies are similar for all alignments, suggesting year-to-year variability in growing conditions for a given county are reasonably well represented by samples from adjacent counties. The accuracies with GDD alignment (RMSE of 0.6–0.8 Mg/ha for corn and 0.20–0.25 Mg/ha for soybean; 5–7% of the mean observed yields) approximate the maximum predictive power of ESI in isolation for the Corn Belt. The leave-one-year-out results are more indicative of operational use, where observations from prior years are used to forecast impacts in the current year. In each case, yield estimates developed from empirical regressions using GDD within-season time adjustments are able to approach the maximum predictive capacity of the ESI, resulting in RMSE of 0.7–0.9 Mg/ha for corn and 0.20–0.26 Mg/ha for soybean, or 5–8% of the observed yield.

6. Discussion

6.1. Comparison to previous Corn Belt yield estimation studies

Historically, most remotely sensed yield estimation efforts have focused on using vegetation indices computed from visible and NIR bands. However, VI-based indices can miss early signals of water stress that may occur during phenologically sensitive stages of crop growth. Over the Ames study domain, Gao et al. (2018) showed that the inter-annual variability of yield could not be well captured by using standard VIs alone, even using high temporal and spatial resolution VI timeseries developed through multi-sensor data fusion. In contrast, ET retrieved from thermal remote sensing inherently incorporates information from visible, NIR and TIR bands and conveys information about biomass accumulation, crop health and soil water supply. Knipper et al. (2019), for example, demonstrate quick response of thermal-based ET retrievals to a controlled stress event in an irrigated vineyard, while NDVI timeseries maps showed a minimal response. More recent narrow-band indices of crop biophysical function such as Solar Induced Fluorescence (SIF) and Photosynthetic Response Index (PRI) show potential for yield estimation (Cheng et al. 2013; Guan et al. 2016), but these

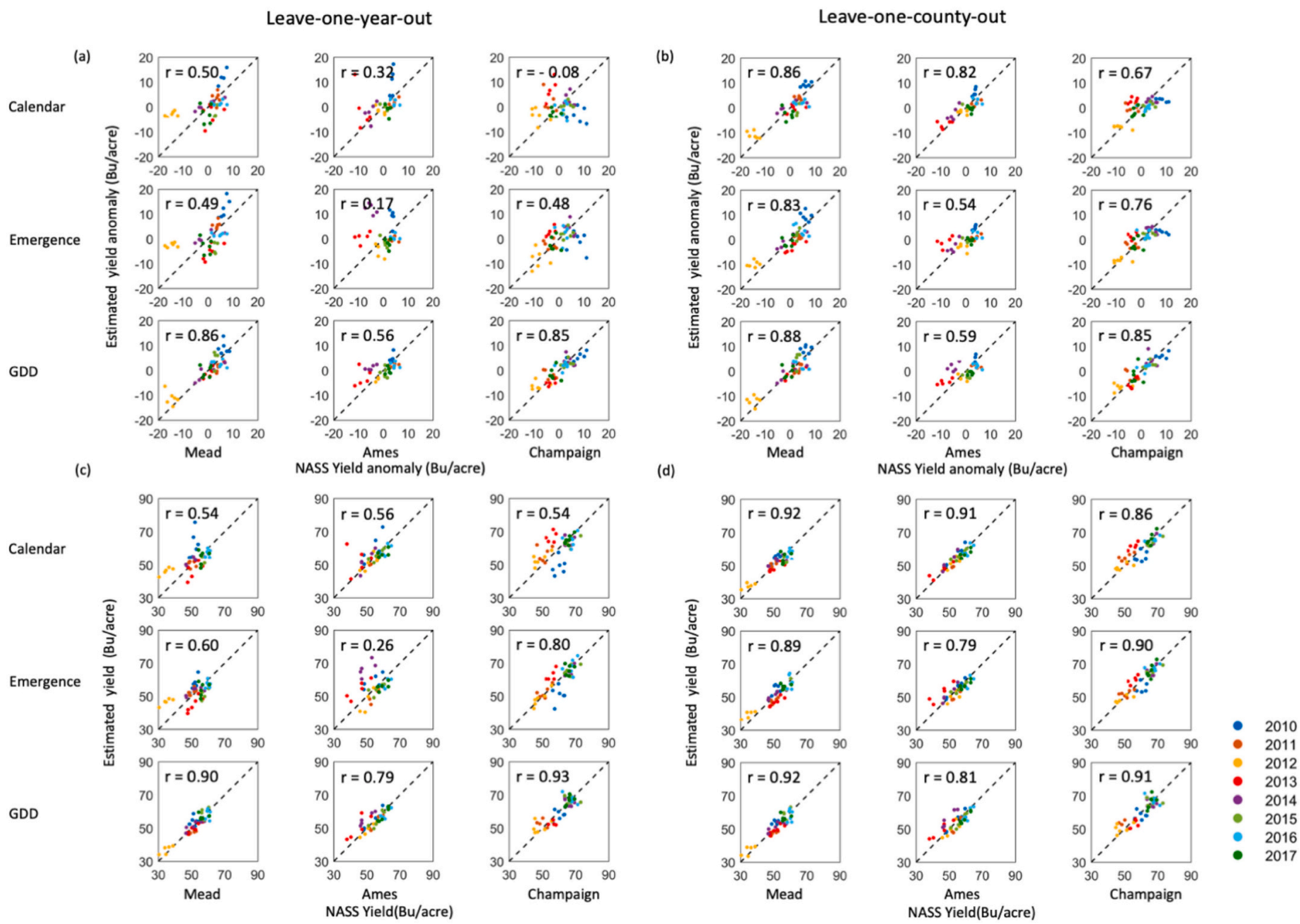

Fig. 8. Comparison of soybean yield anomaly (a, b) and yield (c, d) reported by NASS yield and yields estimated using two bootstrapping strategies: leave-one-year-out (left column) and leave-one-county-out (right column). In each plot, there are three alignments: calendar date (top row in each plot); calendar date with emergence correction using 2010 as a baseline (middle row in each plot); and AGDD (bottom row in each plot) for Mead (left), Ames (middle), and Champaign (right) 2010–2017. Each dot is the yield for one county for a given year. The X-axis is the NASS yield survey data and the Y-axis is the modeled yield.

measurements are not routinely and globally supported by satellites at Landsat-like resolutions.

Table 3 summarizes results from recent studies of corn and soybean yield prediction in the U.S. Corn Belt. Note that all of the county level studies in Table 3 use NASS county level data as validation datasets. Although uncertainties in the NASS county-level yields are not provided, - a common set of validation data lays a foundation for comparison across different studies. Yield estimation accuracies obtained in these studies are shown in terms of R^2 and RMSE where available. In comparison, ESI performance with phenological correction is relatively high, suggesting diagnostic ET timeseries provide utility in forecasting yields at this scale. While the Yang et al. (2018) ESI study obtained higher performance metrics, this earlier study was conducted over a significantly smaller geographic area (5 counties in NE) and a shorter period of record (6 years). In addition, local field observations of crop emergence were used for phenological correction, whereas the methods proposed here used only routinely available state-level reports and may be more indicative of operational performance.

6.2. Importance of full phenological correction

The Yang et al. (2018) 5-year study explored only partial phenological correction to ESI timeseries; namely, adjustments for year-to-year variability in crop emergence date. The results obtained in the 8-year, multi-state study presented here demonstrate that this is not sufficient for wide-scale application over a broad range of seasonal conditions. While emergence corrections serve to reduce spurious anomalies at the start of the growing season, conditions at critical growth stages later in the growing season can remain in disalignment if the temporal axes post-emergence are not further scaled by annual heat accumulation units. This disalignment contributes noise to the correlation curves shown in Fig. 6, and reduces yield predictability for years with significantly different seasonal growing conditions (Figs. 7 and 8). Similar findings were reported by Qian et al. (2019) in monitoring crop condition using NDVI timeseries, who found better agreement between NDVI anomalies and NASS crop condition reports using time axes based on GDD rather than calendar day.

6.3. Improvement of temporal sampling and phenology specification

The critical nature of crop-specific phenological corrections to moisture stress time-series used in yield estimation underscores the utility of mapping ESI at field-scale, thus facilitating separation of signal between different landcover types which may have very different seasonal phenologies. However, one of the most significant limitations thermal-based field-scale ET retrieval is the paucity of medium resolution satellite-based thermal imaging sources. Given the cloud climatology characteristic of the Corn Belt, Landsat alone often does not provide sufficient clear-sky temporal sampling to adequately track changes in crop moisture status. For example, Fig. 4 shows examples at

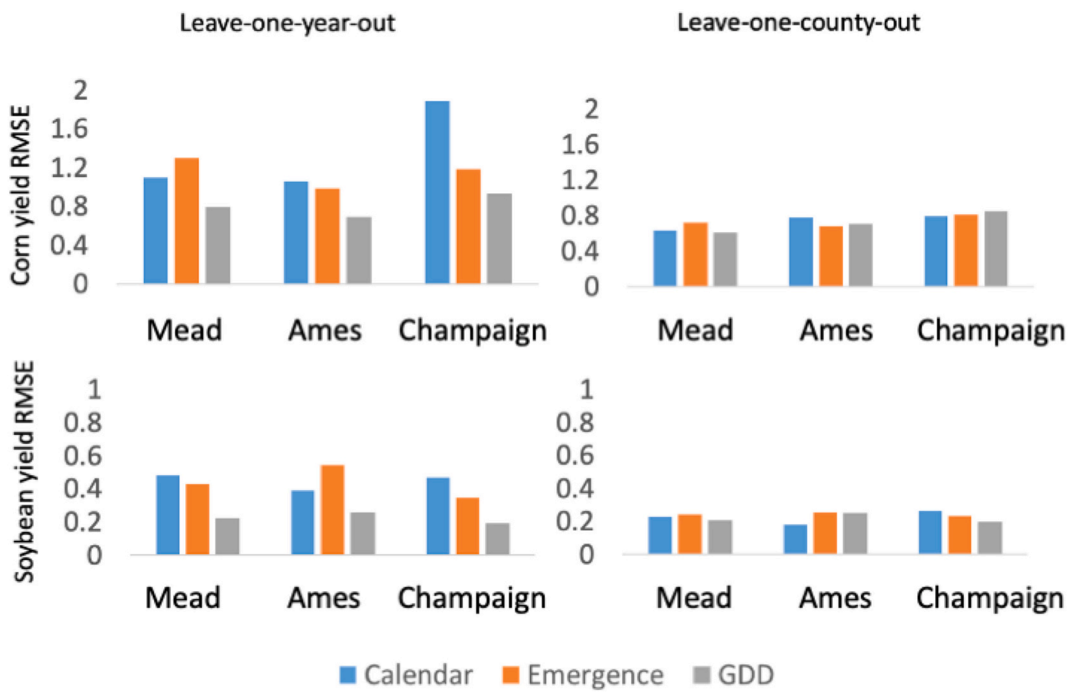

Fig. 9. RMSE values (unit in Mg/ha) for corn and soybean yields across three sites tested on two bootstrapping strategies and three time-axis alignments.

Table 3
Selected studies of remotely sensed corn and soybean yield estimates in the U.S. Corn Belt (CB).

Study	Predictors (resolution)	Yield scale (coverage)	Study span	Methods	Timescale	R^2	RMSE (Mg/ha)
Johnson 2014	MODIS NDVI, daytime LST (250 m/8-day)	County (All CB states)	2006–2012	Machine learning (Cubist)	Calendar	**0.77** 0.71	**1.3** 0.5
Lobell et al. 2015	LAI and Daymet gridded weather (daily/30 m)	Field (IA, IL, IN)	2000–2013	APSIM and multiple linear regression	Calendar	**0.14–0.58** 0.03–0.55	N/A
Guan et al. 2017	PRISM climate data (4 km/daily) Satellite SIF, ET, QuikSCAT, AMSR-E VOD, MODIS EVI (0.05–0.5° /daily-monthly)	County (Core CB counties)	2007–2009	Partial least-square regression	Calendar	**≥ 0.6**	N/A
Gao et al. 2018	EVI2 (daily, 30 m) fused from MODIS, Landsat, Sentinel2 surface reflectance	County (central IA)	2001–2015	Linear regression	Calendar	**0.59** 0.39	**0.8*** 0.4
Li et al. 2019	PRISM climate data (4 km/monthly); MODIS EVI, LST (250 m-1 km/16-day)	County (7 CB states)	2003–2016	Statistical fitting functions	Calendar	**0.79 –0.85**	**0.9–1.04**
Jiang et al. 2020	PRISM climate (2.5 arcmin/daily); MODIS surface reflectance (500 m/8-day)	County (12 CB states)	2006–2015	LSTM model	Emergence	**0.76**	**1.5**
Yang et al. 2018	ESI (daily, 30 m)	County (5 counties in NE)	2010–2015	Linear regression	Emergence	**0.86–0.94**	**0.3–0.5**
Yang et al. 2021 (this study)	ESI (daily, 30 m)	County (17 counties in NE, IL, IA)	2010–2017	Linear regression	GDD	**0.71–0.84** 0.62–0.86	**0.6–0.9** 0.2–0.3

Note: Accuracies are indicated R2 and RMSE. Only best stats are included if studies doing multiple experiments to test the best performance model. Bold fonts are stats for corn and regular fonts are stats for soybean. *RMSE in Gao et al. 2018 was not included in the original paper. Dr. F. Gao computed the RMSE for this manuscript using the same dataset, including 20 counties in central Iowa from 2001 to 2015.

USBr1 (Ames) and USUiC (Champaign) where the peak of the seasonal ET curve in 2013 and 2016 was not captured due to lack of clear Landsat imagery. Work is underway to integrate new sources of thermal data, such as the ECOsystem Spaceborne Thermal Radiometer Experiment on Space Station (ECOSTRESS) and the Visible Infrared Imaging Radiometer Suite (VIIRS) into the ET timeseries generation to better capture the changing evaporative status of the land surface (Anderson et al. 2020). The DMS thermal sharpening toolkit is key to bringing these disparate thermal images to a common 30-m spatial resolution for datacube construction (Xue et al. 2020).

The study also identified potential issues with the use of state-level crop emergence information from NASS Crop Progress reports for phenological corrections at the county scale. Since the 1980s, satellite data have been used to study phenology, such as to estimate growing season duration (Henricksen and Durkin 1986), and to identify crop emergence dates (Badhwar and Thompson 1983). At the regional or global scale, land surface phenology datasets have been produced from various moderate-resolution satellite data sources, including MODIS and VIIRS at the resolution of 500 m (Friedl et al. 2002; Zhang et al. 2003, 2018). Field-scale studies such as Gao et al. (2017) and Bolton et al. (2020) have developed 30-m resolution phenological metrics using Landsat and Sentinel-2 data and related these products to different crop growth stages. Moreover, they demonstrated that remotely sensed "green-up" can be used to retroactively predict emergence date. More recently, Gao et al. (2020) developed a within-season crop emergence mapping approach. The approach requires high temporal and spatial resolution data and has been assessed using the Harmonized Landsat and Sentinel-2 (HLS) data. Operationally, within-season maps of crop emergence and other critical phenological at the field scale could be used to phenologically align ESI timeseries for yield forecasting. Remote sensing can provide spatially explicit phenological information for improving time-axis alignment in ESI at the field scale that the NASS CP report at the state or district (multiple counties) level cannot capture.

7. Conclusion

This study examined the utility of remotely sensed ET in conveying spatially and temporally explicit water stress information for yield prediction. Actual ET and ESI timeseries were generated at 30-m spatial resolution and daily time steps from 2010 to 2017 for three study sites across the U.S. Corn Belt represented by agricultural landscapes around Mead, NE, Ames, IA and Champaign, IL. The satellite ET estimates agreed well with observations from flux towers deployed in these study areas, with a RMSE of 1.2 mm d^{-1} on average. In each study domain, ESI was correlated with anomalies in NASS estimates of county level corn and soybean yields to identify periods where yield was most sensitive to water stress. To examine the role of crop phenology in yield anomaly-ESI correlations, f_{RET} timeseries used to compute ESI were aligned by calendar date, emergence-corrected calendar date, and growing degree days (GDD). Although all three alignments gave high peak correlations between yield anomaly and ESI, the GDD alignment proved more robust if provided with accurate information about the crop emergence date. Peak correlations in the GDD alignment occur during the silking stage for corn and during the reproductive stage for soybean; stages when these crops are particularly sensitive to soil moisture deficiencies.

Yield estimates based on regression equations developed at the times of peak correlation using a bootstrapping approach agree well with NASS county-level crop yield data, with correlation coefficients that range from 0.79 to 0.93 and estimation errors of 5–8% based on GDD alignment and a "leave-one-year-out" bootstrapping strategy. In the cases where correlation coefficients decreased when incorporating state-level phenological information into the ESI alignment, work is underway to evaluate the use of field scale phenology information generated from high spatiotemporal remote sensing data. Given the success in crop yield estimation at multiple locations and years, this study demonstrates the utility of remotely sensed ET at high spatiotemporal resolution in predicting yield response to water stress. Future work will continue to develop strategies for utilizing remotely sensed ET in yield estimation, such as ingesting f_{RET} timeseries maps into gridded crop models through data assimilation.

Author statement

Yang Yang, Martha C. Anderson, Feng Gao formed the concept and workflow of this research. Yang Yang conducted the experiment and led the write-up. Yun Yang, Liang Sun, Wayne Dulaney helped with coding and image processing. David M. Johnson provided insights on NASS data. Chris Hain provided ALEXI ET data. John Prueger, Tilden Meyers, Carl J. Bernacchi, and Caitlin E. Moore provided flux tower data. All the coauthors provided comments on manuscripts.

Declaration of Competing Interest

None.

Acknowledgement

The authors wish to thank Dr. Andy Suyker for providing yield, flux and phenology data for the Mead field sites. We also thank the editor and three anonymous reviewers for providing insightful comments and suggestions, which served to substantially improve the manuscript. This work was partially supported by the NASA's Land Cover and Land Use MuSLI Program (NNH17ZDA001N-LCLUC), the NASA's Science of TERRA, AQUA, and SUOMI NPP Program (NNH17ZDA001N-TASNPP), and the NASA ECOSTRESS Earth Ventures Instrument Program. This research was a contribution from the Long-Term Agroecosystem Research (LTAR) network. LTAR is supported by the United States Department of Agriculture.

References

Allen, R.G., Pereira, L.S., Raes, D., & Smith, M. (1998). Crop Evapotranspiration-Guidelines for Computing Crop Water Requirements-FAO Irrigation and Drainage Paper 56. FAO, Rome, 300, D05109.
Anderson, M., Norman, J., Diak, G., Kustas, W., Mecikalski, J., 1997. A two-source time-integrated model for estimating surface fluxes using thermal infrared remote sensing. Remote Sens. Environ. 60 (2), 195–216.
Anderson, M., Diak, G., Gao, F., Knipper, K., Hain, C., Eichelmann, E., Hemes, K.S., Baldocchi, D., Kustas, W., Yang, Y., 2019. Impact of insolation data source on remote sensing retrievals of evapotranspiration over the California Delta. Remote Sens. 11, 216.
Anderson, M.C., Norman, J., Mecikalski, J.R., Torn, R.D., Kustas, W.P., Basara, J.B., 2004. A multiscale remote sensing model for disaggregating regional fluxes to micrometeorological scales. J. Hydrometeorol. 5, 343–363.
Anderson, M.C., Norman, J.M., Mecikalski, J.R., Otkin, J.A., Kustas, W.P., 2007a. A climatological study of evapotranspiration and moisture stress across the continental United States based on thermal remote sensing: 1. Model formulation. J. Geophys. Res.-Atmos. 112.
Anderson, M.C., Norman, J.M., Mecikalski, J.R., Otkin, J.A., Kustas, W.P., 2007b. A climatological study of evapotranspiration and moisture stress across the continental United States based on thermal remote sensing: 2. Surface moisture climatology. J. Geophys. Res.-Atmos. 112.
Anderson, M.C., Hain, C., Wardlow, B., Pimstein, A., Mecikalski, J.R., Kustas, W.P., 2011. Evaluation of drought indices based on thermal remote sensing of evapotranspiration over the continental United States. J. Clim. 24, 2025–2044.
Anderson, M.C., Kustas, W.P., Alfieri, J.G., Gao, F., Hain, C., Prueger, J.H., Evett, S., Colaizzi, P., Howell, T., Chávez, J.L., 2012. Mapping daily evapotranspiration at Landsat spatial scales during the BEAREX'08 field campaign. Adv. Water Resour. 50, 162–177. https://doi.org/10.1016/j.advwatres.2012.06.005.
Anderson, M.C., Hain, C., Otkin, J., Zhan, X., Mo, K., Svoboda, M., Wardlow, B., Pimstein, A., 2013. An intercomparison of drought indicators based on thermal remote sensing and NLDAS-2 simulations with US drought monitor classifications. J. Hydrometeorol. 14, 1035–1056.
Anderson, M.C., Zolin, C.A., Hain, C.R., Semmens, K., Yilmaz, M.T., Gao, F., 2015. Comparison of satellite-derived LAI and precipitation anomalies over Brazil with a thermal infrared-based evaporative stress index for 2003–2013. J. Hydrol. 526, 287–302.
Anderson, M.C., Hain, C.R., Jurecka, F., Trnka, M., Hlavinka, P., Dulaney, W., Otkin, J. A., Johnson, D., Gao, F., 2016a. Relationships between the evaporative stress index and winter wheat and spring barley yield anomalies in the Czech Republic. Clim. Res. 70, 215–230.
Anderson, M.C., Zolin, C.A., Sentelhas, P.C., Hain, C.R., Semmens, K., Tugrul Yilmaz, M., Gao, F., Otkin, J.A., Tetrault, R., 2016b. The evaporative stress index as an indicator of agricultural drought in Brazil: an assessment based on crop yield impacts. Remote Sens. Environ. 174, 82–99.
Anderson, M.C., Yang, Y., Xue, J., Knipper, K., Yang, Y., Gao, F., Hain, C., Kustas, W.P., Cawse-Nicholson, K., Hulley, G., Fisher, J.B., Alfieri, J., Meyers, T., Prueger, J., Baldocchi, D.D., Rey-Sanchez, C., 2020. Interoperability of ECOSTRESS and Landsat for mapping evapotranspiration time series at sub-field scales. Remote Sens. Environ. 252, 112189.
Badhwar, G., Thompson, D., 1983. Estimating emergence date of spring small grains using Landsat spectral data 1. Agron. J. 75, 75–78.
Bastiaanssen, W.G., Ali, S., 2003. A new crop yield forecasting model based on satellite measurements applied across the Indus Basin, Pakistan. Agric. Ecosyst. Environ. 94, 321–340.
Begg, J.E., Turner, N.C., 1976. Crop water deficits. In: Advances in Agronomy. Elsevier, pp. 161–217.
Berk, A., Bernstein, L.S., Robertson, D.C., 1989. MODTRAN: A Moderate Resolution Model for LOWTRAN 7. GL-TR-89-0122. Air Force Geophysics Lab, Bedford, MA, p. 38.
Bolton, D.K., Gray, J.M., Melaas, E.K., Moon, M., Eklundh, L., Friedl, M.A., 2020. Continental-scale land surface phenology from harmonized Landsat 8 and Sentinel-2 imagery. Remote Sens. Environ. 240, 111685.
Cakir, R., 2004. Effect of water stress at different development stages on vegetative and reproductive growth of corn. Field Crop Res. 89, 1–16.
Cammalleri, C., Anderson, M., Gao, F., Hain, C., Kustas, W., 2013. A data fusion approach for mapping daily evapotranspiration at field scale. Water Resour. Res. 49, 4672–4686.
Cammalleri, C., Anderson, M., Gao, F., Hain, C., Kustas, W., 2014. Mapping daily evapotranspiration at field scales over rainfed and irrigated agricultural areas using remote sensing data fusion. Agric. For. Meteorol. 186, 1–11.
Cheng, Y.B., Middleton, E.M., Zhang, Q., Huemmrich, K.F., Campbell, P.K., Cook, B.D., Kustas, W.P., Daughtry, C.S., 2013. Integrating solar induced fluorescence and the photochemical reflectance index for estimating gross primary production in a cornfield. Remote Sensing 5 (12), 6857–6879.
Cook, M., Schott, J.R., Mandel, J., Raqueno, N., 2014. Development of an operational calibration methodology for the Landsat thermal data archive and initial testing of the atmospheric compensation component of a land surface temperature (LST) pro-

duct from the archive. Remote Sens. 6, 11244–11266. https://doi.org/10.3390/rs61111244.
Claassen, M., Shaw, R.H., 1970. Water deficit effects on corn. II. Grain components 1. Agron. J. 62, 652–655.
Deines, J.M., Kendall, A.D., Crowley, M.A., Rapp, J., Cardille, J.A., Hyndman, D.W., 2019. Mapping three decades of annual irrigation across the US High Plains aquifer using Landsat and Google earth engine. Remote Sens. Environ. 233, 111400.
Dogan, E., Kirnak, H., Copur, O., 2007. Deficit irrigations during soybean reproductive stages and CROPGRO-soybean simulations under semi-arid climatic conditions. Field Crop Res. 103, 154–159.
Doorenbos, J., Kassam, A., 1979. Yield response to water. In: Irrigation and Drainage Paper, p. 257.
Duvick, D., 2005. Genetic progress in yield of United States maize (*Zea mays* L.). Maydica 50, 193.
Egli, D.B., 2008. Comparison of corn and soybean yields in the United States: historical trends and future prospects. Agron. J. 100, S–79-S-88.
Friedl, M.A., McIver, D.K., Hodges, J.C., Zhang, X.Y., Muchoney, D., Strahler, A.H., Woodcock, C.E., Gopal, S., Schneider, A., Cooper, A., 2002. Global land cover mapping from MODIS: algorithms and early results. Remote Sens. Environ. 83, 287–302.
Gao, F., Masek, J., Schwaller, M., Hall, F., 2006. On the blending of the Landsat and MODIS surface reflectance: predicting daily Landsat surface reflectance. IEEE Trans. Geosci. Remote Sens. 44, 2207–2218.
Gao, F., Kustas, W.P., Anderson, M.C., 2012a. A data mining approach for sharpening thermal satellite imagery over land. Remote Sens. 4, 3287–3319.
Gao, F., Anderson, M.C., Kustas, W.P., Wang, Y., 2012b. Simple method for retrieving leaf area index from Landsat using MODIS leaf area index products as reference. J. Appl. Remote. Sens. 6, 063554.
Gao, F., Hilker, T., Zhu, X., Anderson, M., Masek, J., Wang, P., Yang, Y., 2015. Fusing Landsat and MODIS data for vegetation monitoring. IEEE Geosci. Remote Sens. Magaz 3, 47–60.
Gao, F., Anderson, M.C., Zhang, X., Yang, Z., Alfieri, J.G., Kustas, W.P., Mueller, R., Johnson, D.M., Prueger, J.H., 2017. Toward mapping crop progress at field scales through fusion of Landsat and MODIS imagery. Remote Sens. Environ. 188, 9–25.
Gao, F., Anderson, M., Daughtry, C., Johnson, D., 2018. Assessing the variability of corn and soybean yields in Central Iowa using high spatiotemporal resolution multi-satellite imagery. Remote Sens. 10, 1489.
Gao, F., Anderson, M., Daughtry, C., Karnieli, A., Hively, D., Kustas, W., 2020. A within-season approach for detecting early growth stages in corn and soybean using high temporal and spatial resolution imagery. Remote Sens. Environ. 242, 111752.
Gilmore, E., Rogers, J., 1958. Heat units as a method of measuring maturity in corn. Agron. J. 50, 611–615.
Grassini, P., van Bussel, L.G., Van Wart, J., Wolf, J., Claessens, L., Yang, H., Boogaard, H., de Groot, H., van Ittersum, M.K., Cassman, K.G., 2015. How good is good enough? Data requirements for reliable crop yield simulations and yield-gap analysis. Field Crop Res. 177, 49–63.
Guan, K., Berry, J.A., Zhang, Y., Joiner, J., Guanter, L., Badgley, G., Lobell, D.B., 2016. Improving the monitoring of crop productivity using spaceborne solar-induced fluorescence. Global change biology 22 (2), 716–726.
Guan, K., Wu, J., Kimball, J.S., Anderson, M.C., Frolking, S., Li, B., Hain, C.R., Lobell, D. B., 2017. The shared and unique values of optical, fluorescence, thermal and microwave satellite data for estimating large-scale crop yields. Remote sensing of environment 199, 333–349.
Hain, C.R., Anderson, M.C., 2017. Estimating morning change in land surface temperature from MODIS day/night observations: applications for surface energy balance modeling. Geophys. Res. Lett. 44, 9723–9733.
Hain, C.R., Mecikalski, J.R., Anderson, M.C., 2009. Retrieval of an available water-based soil moisture proxy from thermal infrared remote sensing. Part I: Methodology and validation. J. Hydrometeorol. 10, 665–683.
Hain, C.R., Crow, W.T., Mecikalski, J.R., Anderson, M.C., Holmes, T., 2011. An intercomparison of available soil moisture estimates from thermal infrared and passive microwave remote sensing and land surface modeling. J. Geophys. Res.-Atmos. 116.
Hatfield, J., Jaynes, D., Burkart, M., Cambardella, C., Moorman, T., Prueger, J., Smith, M., 1999. Water quality in Walnut Creek watershed: setting and farming practices. J. Environ. Qual. 28, 11–24.
Henricksen, B., Durkin, J., 1986. Growing period and drought early warning in Africa using satellite data. Int. J. Remote Sens. 7, 1583–1608.
Huang, J., Ma, H., Su, W., Zhang, X., Huang, Y., Fan, J., Wu, W., 2015. Jointly assimilating MODIS LAI and ET products into the SWAP model for winter wheat yield estimation. IEEE J. Sel. Topics Appl. Earth Observ. Remote Sens. 8, 4060–4071.
Jensen, M.E., 1968. Water Consumption by Agricultural Plants (Chapter 1).
Jiang, H., Hu, H., Zhong, R., Xu, J., Xu, J., Huang, J., Wang, S., Ying, Y., Lin, T., 2020. A deep learning approach to conflating heterogeneous geospatial data for corn yield estimation: a case study of the US Corn Belt at the county level. Glob. Chang. Biol. 26, 1754–1766.
Johnson, D.M., 2014. An assessment of pre-and within-season remotely sensed variables for forecasting corn and soybean yields in the United States. Remote Sensing of Environment 141, 116–128.
Knipper, K.R., Kustas, W.P., Anderson, M.C., Alfieri, J.G., Prueger, J.H., Hain, C.R., Gao, F., Yang, Y., McKee, L.G., Nieto, H., Hipps, L.E., Alsina, M.M., Sanchez, L., 2019. Evapotranspiration estimates derived using thermal-based satellite remote sensing and data fusion for irrigation management in California vineyards. Irrig. Sci. 37, 431–449.
Korte, L., Specht, J., Williams, J., Sorensen, R., 1983. Irrigation of soybean genotypes during reproductive ontogeny II. Yield component responses 1. Crop Sci. 23, 528–533.
Kucharik, C.J., Ramankutty, N., 2005. Trends and variability in US corn yields over the twentieth century. Earth Interact. 9, 1–29.
Kustas, W.P., Norman, J.M., 1997. A two-source approach for estimating turbulent fluxes using multiple angle thermal infrared observations. Water Resour. Res. 33, 1495–1508. https://doi.org/10.1029/97WR00704.
Kustas, W.P., Norman, J.M., 1999. Evaluation of soil and vegetation heat flux predictions using a simple two-source model with radiometric temperatures for partial canopy cover. Agric. For. Meteorol. 94, 13–29.
Li, Y., Guan, K., Yu, A., Peng, B., Zhao, L., Li, B., Peng, J., 2019. Toward building a transparent statistical model for improving crop yield prediction: Modeling rainfed corn in the US. Field Crops Research 234, 55–65.
Liu, X., Chen, F., Barlage, M., Zhou, G., Niyogi, D., 2016. Noah-MP-crop: introducing dynamic crop growth in the Noah-MP land surface model. J. Geophys. Res.-Atmos. 121, 13,953–913,972.
Lobell, D.B., Thau, D., Seifert, C., Engle, E., Little, B., 2015. A scalable satellite-based crop yield mapper. Remote Sensing of Environment 164, 324–333.
Lu, J., Carbone, G.J., Gao, P., 2017. Detrending crop yield data for spatial visualization of drought impacts in the United States, 1895–2014. Agric. For. Meteorol. 237, 196–208.
McNaughton, K., Spriggs, T., 1986. A mixed-layer model for regional evaporation. Bound.-Layer Meteorol. 34, 243–262.
Meyers, T.P., Hollinger, S.E., 2004. An assessment of storage terms in the surface energy balance of maize and soybean. Agric. For. Meteorol. 125, 105–115.
Mishra, V., Cruise, J.F., Mecikalski, J.R., Hain, C.R., Anderson, M.C., 2013. A remote-sensing driven tool for estimating crop stress and yields. Remote Sens. 5, 3331–3356.
Mladenova, I.E., Bolten, J.D., Crow, W.T., Anderson, M.C., Hain, C.R., Johnson, D.M., Mueller, R., 2017. Intercomparison of soil moisture, evaporative stress, and vegetation indices for estimating corn and soybean yields over the US. IEEE J. Sel. Topics Appl. Earth Observ. Remote Sens. 10, 1328–1343.
Moran, M.S., 2004. Thermal infrared measurement as an indicator of plant ecosystem health. Thermal Remote Sens. Land Surf. Proces. 257–282.
Myneni, R., Knyazikhin, Y., Park, T., 2015. MCD15A3H MODIS/Terra+Aqua Leaf Area Index/FPAR 4-day L4 Global 500m SIN Grid V006. NASA EOSDIS Land Processes DAAC. https://doi.org/10.5067/MODIS/MCD15A3H.006.
NASS CDL, 2010-2017. https://www.nass.usda.gov/Research_and_Science/Cropland/Release/index.php (last accessed 20 October 2019).
NASS CP, 2010-2017. http://www.nass.usda.gov/Publications/National_Crop_Progress/ (last accessed 30 October 2019).
NASS Quick Stats, 2010-2019. https://quickstats.nass.usda.gov/ (last accessed 10 March 2020).
National Academies of Sciences, Engineering, & Medicine, 2017. Improving Crop Estimates by Integrating Multiple Data Sources. National Academies Press.
Neild, R.E., Newman, J.E., 1987. Growing Season Characteristics and Requirements in the Corn Belt. Cooperative Extension Service. Iowa State University.
Norman, J., Anderson, M., Kustas, W., French, A., Mecikalski, J., Torn, R., Diak, G., Schmugge, T., Tanner, B., 2003. Remote sensing of surface energy fluxes at 101-m pixel resolutions. Water Resour. Res. 39.
Norman, J.M., Kustas, W.P., Humes, K.S., 1995. Source approach for estimating soil and vegetation energy fluxes in observations of directional radiometric surface temperature. Agric. For. Meteorol. 77, 263–293.
Otkin, J.A., Anderson, M.C., Hain, C., Mladenova, I.E., Basara, J.B., Svoboda, M., 2013. Examining rapid onset drought development using the thermal infrared–based evaporative stress index. J. Hydrometeorol. 14, 1057–1074.
Otkin, J.A., Anderson, M.C., Hain, C., Svoboda, M., 2014. Examining the relationship between drought development and rapid changes in the evaporative stress index. J. Hydrometeorol. 15, 938–956.
Otkin, J.A., Anderson, M.C., Hain, C., Svoboda, M., Johnson, D., Mueller, R., Tadesse, T., Wardlow, B., Brown, J., 2016. Assessing the evolution of soil moisture and vegetation conditions during the 2012 United States flash drought. Agric. For. Meteorol. 218, 230–242.
Pedersen, P., Kumudini, S., Board, J., Conley, S., 2004. Soybean Growth and Development. Iowa State University, University Extension Ames, IA.
Pejić, B., Maksimović, L., Cimpeanu, S., Bucur, D., Milić, S., Ćupina, B., 2011. Response of soybean to water stress at specific growth stages. J. Food Agric. Environ. 9, 280–284.
Prueger, J.H., Kustas, W.P., 2005. Aerodynamic methods for estimating turbulent fluxes. Micrometeorology in agricultural systems 47, 407–436.
Qian, Y., Yang, Z., Di, L., Rahman, M., Tan, Z., Xue, L., Gao, F., Yu, E.G., Zhang, X., 2019. Crop growth condition assessment at county scale based on heat-aligned growth stages. Remote Sens. 11, 2439.
Ritchie, S., Hanway, J., Benson, G., 1997. How a Corn Plants Develops. In: Spec. Publ. 48. Iowa State Univ. Coop. Ext. Serv, Ames.
Saha, S., Moorthi, S., Wu, X., Wang, J., Nadiga, S., Tripp, P., Behringer, D., Hou, Y.-T., Chuang, H.-Y., Iredell, M., 2014. The NCEP climate forecast system version 2. J. Clim. 27, 2185–2208.
Seguin, B., Becker, F., Phulpin, T., Gu, X., Guyot, G., Kerr, Y., King, C., Lagouarde, J., Ottlé, C., Stoll, M., 1999. IRSUTE: a minisatellite project for land surface heat flux estimation from field to regional scale. Remote Sens. Environ. 68, 357–369.
Semmens, K.A., Anderson, M.C., Kustas, W.P., Gao, F., Alfieri, J.G., McKee, L., Prueger, J. H., Hain, C.R., Cammalleri, C., Yang, Y., 2016. Monitoring daily evapotranspiration over two California vineyards using Landsat 8 in a multi-sensor data fusion approach. Remote Sens. Environ. 185, 155–170.

Skaggs, K.E., Irmak, S., 2012. Long-term trends in air temperature distribution and extremes, growing degree-days, and spring and fall frosts for climate impact assessments on agricultural practices in Nebraska. J. Appl. Meteorol. Climatol. 51, 2060–2073.

Sun, L., Anderson, M.C., Gao, F., Hain, C., Alfieri, J.G., Sharifi, A., McCarty, G.W., Yang, Y., Yang, Y., Kustas, W.P., 2017. Investigating water use over the C hoptank R iver W atershed using a multisatellite data fusion approach. Water Resour. Res. 53, 5298–5319.

Suyker, A., Verma, S., 2009. Evapotranspiration of irrigated and rainfed maize–soybean cropping systems. Agric. For. Meteorol. 149, 443–452.

Suyker, A., Verma, S., Burba, G., Arkebauer, T., Walters, D., Hubbard, K., 2004. Growing season carbon dioxide exchange in irrigated and rainfed maize. Agric. For. Meteorol. 124, 1–13.

Tadesse, T., Senay, G.B., Berhan, G., Regassa, T., Beyene, S., 2015. Evaluating a satellite-based seasonal evapotranspiration product and identifying its relationship with other satellite-derived products and crop yield: a case study for Ethiopia. Int. J. Appl. Earth Obs. Geoinf. 40, 39–54.

Teixeira, D.C., Antônio, H., Scherer-Warren, M., Hernandez, F.B., Andrade, R.G., Leivas, J.F., 2013. Large-scale water productivity assessments with MODIS images in a changing semi-arid environment: a Brazilian case study. Remote Sens. 5, 5783–5804.

Twine, T.E., Kustas, W., Norman, J., Cook, D., Houser, P., Meyers, T., Prueger, J., Starks, P., Wesely, M., 2000. Correcting eddy-covariance flux underestimates over a grassland. Agric. For. Meteorol. 103, 279–300.

Wan, Z., Hook, S., Hulley, G., 2015. MOD11 L2 MODIS/Terra Land Surface Temperature/Emissivity 5-min L2 Swath 1 Km V006. NASA EOSDIS Land Processes DAAC.

Wang, Z., Schaaf, C.B., Sun, Q., Shuai, Y., Román, M.O., 2018. Capturing rapid land surface dynamics with collection V006 MODIS BRDF/NBAR/albedo (MCD43) products. Remote Sens. Environ. 207, 50–64.

Wilson, J.H., 1968. Water relations of maize. Effects of severe soil moisture stress imposed at different stages of growth on grain yields of maize. Rhod. J. Agric. Res. 6, 103–105.

Wilson, K., Goldstein, A., Falge, E., Aubinet, M., Baldocchi, D., Berbigier, P., Bernhofer, C., Ceulemans, R., Dolman, H., Field, C., 2002. Energy balance closure at FLUXNET sites. Agric. For. Meteorol. 113, 223–243.

Xue, J., Anderson, M.C., Gao, F., Hain, C., Sun, L., Yang, Y., Knipper, K.R., Kustas, W.P., Torres-Rua, A., Schull, M.A., 2020. Sharpening ECOSTRESS and VIIRS land surface temperature using harmonized Landsat-sentinel surface reflectance. Remote Sens. Environ. 251, 112055.

Yang, Y., Anderson, M., Gao, F., Hain, C., Kustas, W., Meyers, T., Crow, W., Finocchiaro, R., Otkin, J., Sun, L., 2017. Impact of tile drainage on evapotranspiration in South Dakota, USA, based on high spatiotemporal resolution evapotranspiration time series from a multisatellite data fusion system. IEEE J. Sel. Topics Appl. Earth Observ. Remote Sens. 10, 2550–2564.

Yang, Y., Anderson, M.C., Gao, F., Wardlow, B., Hain, C.R., Otkin, J.A., Alfieri, J., Yang, Y., Sun, L., Dulaney, W., 2018. Field-scale mapping of evaporative stress indicators of crop yield: an application over Mead, NE, USA. Remote Sens. Environ. 210, 387–402.

Yang, Y., Anderson, M., Gao, F., Johnson, D., Yang, Y., Sun, L., Dulaney, W., Hain, C., Otkin, J., Prueger, J.,Meyers, T., Bernacchi, C., Moore, C., 2021. Phenological corrections to a field-scale, ET-based crop stress indicator: An application to yield forecasting across the U.S. Corn Belt. Remote Sensing of Environment, in press.

Zhang, X., Friedl, M.A., Schaaf, C.B., Strahler, A.H., Hodges, J.C., Gao, F., Reed, B.C., Huete, A., 2003. Monitoring vegetation phenology using MODIS. Remote Sens. Environ. 84, 471–475.

Zhang, X., Liu, L., Liu, Y., Jayavelu, S., Wang, J., Moon, M., Henebry, G.M., Friedl, M.A., Schaaf, C.B., 2018. Generation and evaluation of the VIIRS land surface phenology product. Remote Sens. Environ. 216, 212–229.